

REDUCTION PIPELINE FOR ROBOTIC TELESCOPE OBSERVATIONS OF
GRAVITATIONAL WAVES ELECTROMAGNETIC COUNTERPARTS AND
OTHER TRANSIENTS

AS
36
2019
PHYS
.965

A thesis presented to the faculty of
San Francisco State University
In partial fulfilment of
The Requirements for
The Degree

Master of Science
In
Physics with Concentration in Astronomy

by

Priyadarshini Gokul dass

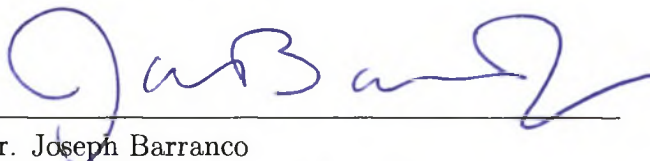
San Francisco, California

August 2019

Copyright by
Priyadarshini Gokul dass
2019

CERTIFICATION OF APPROVAL

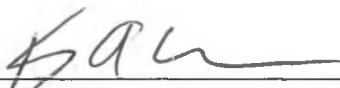
I certify that I have read *REDUCTION PIPELINE FOR ROBOTIC TELESCOPE OBSERVATIONS OF GRAVITATIONAL WAVES ELECTROMAGNETIC COUNTERPARTS AND OTHER TRANSIENTS* by Priyadarshini Gokul dass and that in my opinion this work meets the criteria for approving a thesis submitted in partial fulfillment of the requirements for the degree: Master of Science in Physics with Concentration in Astronomy at San Francisco State University.



Dr. Joseph Barranco
Professor of Physics & Astronomy



Dr. Antonino Cucchiara
Assistant Professor of Physics & Astronomy



Dr. Kimberly Coble
Professor of Physics & Astronomy

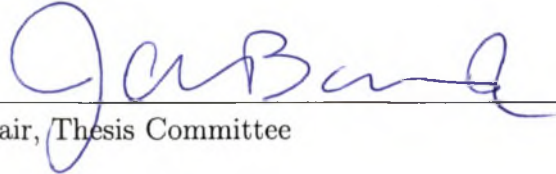
REDUCTION PIPELINE FOR ROBOTIC TELESCOPE OBSERVATIONS OF
GRAVITATIONAL WAVES ELECTROMAGNETIC COUNTERPARTS AND
OTHER TRANSIENTS

Priyadarshini Gokul dass
San Francisco State University
2019

Gravitational waves (GW) are produced by the merger of two compact objects. Observations and analysis of gravitational waves and their electromagnetic counterparts produced in space will help in studying the compact objects and regions of space where strong gravitational field are produced and General Relativity is at play with an unprecedented level of detail. Thanks to the early detection of GW by the LIGO/VIRGO experiments we now know that some of them are connected with the Gamma-ray Bursts (GRB) class of fast astronomical transients. The goal of this project is to create a reduction pipeline for processing the optical images obtained using the RCT (Robotically-Controlled Telescope) at Kitt Peak and the Virgin Island Robotic Telescope (VIRT). RCT and VIRT take images of the night sky autonomously, responding quickly to the discovery of the GRBs (within few minutes). Studying these images will provide a deeper understanding of GRBs and correlation with the GW emitter. Based on the RCT data, a reduction pipeline will be coded to get the final processed science image in real time. Calibration and science images obtained from RCT/VIRT can be processed using the reduction

pipeline to get the median of bias and flat images and this processed flat image is further normalized to get a detector response function. Finally, these data can be used to get the final science processed image. The pipeline will be used to automatically analyze the data without any human interaction on RCT/VIRT and will allow immediate data analysis within a few minutes of the GW/GRB discovery, enabling further and more detailed observations from other facilities (e.g. optical spectroscopy, deeper optical/NIR imaging).

I certify that the Abstract is a correct representation of the content of this thesis.


Chair, Thesis Committee

08/06/2019
Date

ACKNOWLEDGMENTS

Foremost, I would like to express my sincere gratitude to my advisor Assistant Prof. Antonino Cucchiara for the continuous support of my Master's study and research, for his patience, motivation, enthusiasm, and immense knowledge. His guidance helped me in all the time of research and writing of this thesis. He consistently allowed this paper to be my work but steered me in the right the direction whenever he thought I needed it. I could not have imagined having a better advisor and mentor for my Master's study.

Besides my advisor, I would like to thank the rest of my thesis committee: Prof. Kimberly Coble, and Prof. Joseph Barranco, for their encouragement, support, insightful comments, and hard questions.

I would like to acknowledge my friends from the Physics and Astronomy department at San Francisco State University for their emotional support, encouragement, and understanding. The time spent at the computer room studying with everyone greatly helped me to perform well in my Master's career. You supported me greatly and were always willing to help me.

A special thanks to Caroline Alcantara for being the backbone of the Physics and Astronomy department at San Francisco State University. Also, I would like to thank my parents, my sister and my friend Varun for their wise counsel and sympathetic ear. You are always there for me.

Finally, there are my other friends, who were of great help during my life as Master's student. Talking to all of them while away from home helped me feel closer to home.

TABLE OF CONTENTS

1	Introduction	1
1.1	Gamma Ray Bursts	2
1.1.1	Long Gamma Ray Burst	7
1.1.2	Short Gamma Ray Burst	8
1.2	Gravitational Waves	9
1.3	Fast Radio Burst	13
2	Robotic Telescope	16
2.1	Robotically Controlled Telescope	17
2.2	Virgin Island Robotic Telescope	18
2.3	Charge Couple Device(CCD)	20
2.4	Photometric System	22
3	Data Reduction Pipeline	24
3.1	Bias	25
3.2	Flat	25
3.3	Science	26
3.4	Processed Image	26
4	Data Analysis	31
5	Conclusion	51

Bibliography 53

LIST OF TABLES

Table	Page
1.1 The table shows the predictions and expectations for short GRB progenitor models. Ref[21]	10
4.1 Table below contains the list of GRBs analyzed, it's redshift and the telescope used to capture the science image of the particular GRB. . .	33
4.2 Table shows the data obtained from the GCN archive about GRB171010A detected by RTC.	33
4.3 Table shows the data obtained from the GCN archive about GRB171205A detected by RTC.	34
4.4 Table shows the data obtained from the GCN archive about GRB180224A detected by RTC.	35
4.5 Table shows the data obtained from the GCN archive about GRB180205A detected by RTC.	35
4.6 Table shows the data obtained from the GCN archive about GRB171120A detected by RTC.	36
4.7 Table shows the data obtained from the GCN archive about GRB190627A detected by VIRT.	36
4.8 Table shows the data obtained from the master science image of GRB171010A detected by RTC.	37
4.9 Table shows the data obtained from the master science image of GRB171205A detected by RTC.	37

4.10	Table shows the data obtained from the master science image of GRB180224A detected by RTC.	37
4.11	Table shows the data obtained from the master science image of GRB180205A detected by RTC.	38
4.12	Table shows the data obtained from the master science image of GRB171120A detected by RTC.	38
4.13	Table shows the data obtained from the master science image of GRB190627A detected by VIRT.	38

LIST OF FIGURES

Figure	Page
1.1 The figure shows the All-Sky plot of 2704 gamma ray burst locations detected by BATSE instrument over a nine-year period of observations. The bursts are isotropically distributed on the sky with a fluence of about 50-300 KeV. source: (NASA BATSE webpage) . . .	5
1.2 Schematic picture of BH hyperaccretion inflow-outflow model for LGRBs and ULGRBs. source: [34]	8
1.3 a)Image shows the artistic rendering of the gravitational wave. source:(Swinburne Astronomy Production). b)Image shows the aerial view of the VIRGO detector. VIRGO is the third detector to detect the gravitational wave. source:(ligo.caltech.edu/image)	11
1.4 A full picture of compact binary systems. The figure shows different compact binary systems and potential corresponding observations. source: [20](Dong et al. 2018)	13
1.5 An Aitoff projected map of current FRBs in the Galactic coordinates, in which the black dashed line denotes the celestial equator. The detections are from these telescopes: Parkes radio telescope (red circles), Arecibo radio telescope (cyan thin diamond), Green Bank Telescope (green square), UTMOST (yellow down-pointing triangles), ASKAP (blue up-pointing triangles). In particular, the repeater (FRB 121102) is marked by a cyan star. source: [33](Yi et al. 2018)	15

2.1	Image of a) Robotic controlled telescope at Kitt Peak and b) Virgin Island Robotic Telescope at US Virgin Island.	20
2.2	Plot shows the passband of Jonson–cousin filter. source: [35]	23
3.1	The flowchart shows the pipeline process for reducing the images to obtain the processed master science image which will be analyzed further to study the GRBs.	28
3.2	a) The raw bias image taken with shutter of the camera closed. It is used to reduce the variations in the signal due to camera sensors. The two black stripes on the right and left are due to the instrumental error. b) Bias image with the stripe removed on either side.	29
3.3	a) Raw flat Images taken in different filters B, V, R respectively. Flat images are taken with the source evenly illuminated. The grey stripes are due to the instrumental errors. This raw image is then processed to get median and then normalized to get same intensity level.	29
3.4	The figure shows the raw science image taken by the robotic controller telescope (RCT) at Kitt Peak using V filter.	30

3.5	The image at the top left is a Median Bias image. A set of raw bias images are processed to get the median of the raw images which will eliminate readout noise in the science image. The image at the top right is the median flat image. A set of raw flat images are processed to the median flat. The image at the bottom left is the normalized flat image. The median flat image is normalized to get even intensity of light at every pixel. The image at the bottom right is the final master science image.	30
4.1	The plot shows the light curve of GRB171010A plotted using the data obtained from the GCN archive. The x-axis shows the time (sec) at which the GRB was observed by the observatories and the y-axis shows the flux in mJy. The magnitude and error in magnitude obtained from the GCN archive were corrected for its galactic extinction and then converted into its flux value [14].	39
4.2	The plot shows the light curve of GRB171120A plotted using the data obtained from the GCN archive. The x-axis shows the time (sec) at which the GRB was observed by the observatories and the y-axis shows the flux in mJy. The magnitude and error in magnitude obtained from the GCN archive were corrected for its galactic extinction and then converted into its flux value.	40

- 4.3 The plot shows the light curve of GRB171205A plotted using the data obtained from the GCN archive. The x-axis shows the time (sec) at which the GRB was observed by the observatories and the y-axis shows the flux in mJy. The magnitude and error in magnitude obtained from the GCN archive were corrected for its galactic extinction and then converted into its flux value. 41
- 4.4 The plot shows the light curve of GRB180205A plotted using the data obtained from the GCN archive. The x-axis shows the time (sec) at which the GRB was observed by the observatories and the y-axis shows the flux in mJy. The magnitude and error in magnitude obtained from the GCN archive were corrected for its galactic extinction and then converted into its flux value. 42
- 4.5 The plot shows the light curve of GRB180224A plotted using the data obtained from the GCN archive. The x-axis shows the time (sec) at which the GRB was observed by the observatories and the y-axis shows the flux in mJy. The magnitude and error in magnitude obtained from the GCN archive were corrected for its galactic extinction and then converted into its flux value. 43

4.6	The plot shows the light curve of GRB190627A plotted using the data obtained from the GCN archive. The x-axis shows the time (sec) at which the GRB was observed by the observatories and the y-axis shows the flux in mJy. The magnitude and error in magnitude obtained from the GCN archive were corrected for its galactic extinction and then converted into its flux value.	44
4.7	The plot shows the light curve of GRB171010A plotted using the data collected from the processed science image using SExtractor. The images are captured by the robotically controlled telescope at Kitt Peak. The x-axis shows the time (sec) at which the GRB was observed by the RCT and the y-axis shows the flux in mJy. The upper limit is calculated using the background count value of the area near the RA and Dec at which the source was detected.	45
4.8	The plot shows the light curve of GRB171120A plotted using the data collected from the processed science image using SExtractor. The images are captured by the robotically controlled telescope at Kitt Peak. The x-axis shows the time (sec) at which the GRB was observed by the RCT and the y-axis shows the flux in mJy. The upper limit is calculated using the background count value of the area near the RA and Dec at which the source was detected.	46

- 4.9 The plot shows the light curve of GRB171205A plotted using the data collected from the processed science image using SExtractor. The images are captured by the robotically controlled telescope at Kitt Peak. The x-axis shows the time (sec) at which the GRB was observed by the RCT and the y-axis shows the flux in mJy. The upper limit is calculated using the background count value of the area near the RA and Dec at which the source was detected. 47
- 4.10 The plot shows the light curve of GRB180205A plotted using the data collected from the processed science image using SExtractor. The images are captured by the robotically controlled telescope at Kitt Peak. The x-axis shows the time (sec) at which the GRB was observed by the RCT and the y-axis shows the flux in mJy. The upper limit is calculated using the background count value of the area near the RA and Dec at which the source was detected. 48
- 4.11 The plot shows the light curve of GRB180224A plotted using the data collected from the processed science image using SExtractor. The images are captured by the robotically controlled telescope at Kitt Peak. The x-axis shows the time (sec) at which the GRB was observed by the RCT and the y-axis shows the flux in mJy. The upper limit is calculated using the background count value of the area near the RA and Dec at which the source was detected. 49

4.12 The plot shows the light curve of GRB190627A plotted using the data collected from the processed science image using SExtractor. The images are captured by the robotically controlled telescope at Kitt Peak. The x-axis shows the time (sec) at which the GRB was observed by the RCT and the y-axis shows the flux in mJy. The upper limit is calculated using the background count value of the area near the RA and Dec at which the source was detected. 50

Chapter 1

Introduction

The invention of the telescope by astronomer Galileo Galilei in 1609 revolutionized the field of astronomy as it paved the way to view and observe distant events. Later in 1668, Sir Isaac Newton built the first reflecting telescope called the Newtonian reflector. By the 20th century, development of the telescopes increased greatly and had a wide range of wavelength from radio to gamma-rays. This evolution of the telescopes allowed the astronomer to discover and observe the populations of rare and luminous transients such as a supernova, variable stars, etc.

Transients are astronomical phenomena that change in brightness over a period of time. Before the invention of telescopes, such astronomical events from within or near the Milky Way galaxy were very rare to observe. With the development of telescopes, the study of transients escalated as it helps to understand the process which produced our universe. Most transients are found to occur at a cosmic dis-

tance which poses a great challenge to study them properly. The field of transient and time-domain astronomy is developing greatly which improves our capacity to find and identify fast transients. Many of these transients are well explained by phenomena such as shock-breakout flashes from supernovae (e.g., Ofek et al. 2010; Shivvers et al. 2016; Arcavi et al. 2017), early emission from relativistic supernovae (Whitesides et al. 2017), or the shockwave afterglows from gamma-ray bursts (Cenko et al. 2013, 2015; Stalder et al. 2017; Bhalerao et al. 2017) [28].

Some of the recent pinnacles of time-domain and transient astronomy include i) the discovery of gamma-ray burst at redshift of 8-9.5 (the most distant object in the universe); ii) relativistic jet formation and shock breakouts in supernova; iii) the detection of jets from the tidal destruction of a stray star by a supermassive black hole; iv) discovery of most luminous known supernovae with an energy scale that requires new exotic explosion mechanism [1].

1.1 Gamma Ray Bursts

Gamma Ray Bursts are the intensely bright and powerful radiation that occur in the night sky due to the collapse of massive stars or the merging process of two compact objects (like black holes or neutron stars). This resulting radiation is detected as a transient event that releases high energy X-rays for decades and gamma rays for about millisecond to several hours. They typically release about $10^{53} - 10^{54}$ erg of energy within seconds. GRB is classified as long-GRB and short-GRB depending

upon the burst duration and progenitors. The spatial distributions of GRB are isotropic which shows that they are billions of cosmological years away. Figure 1.1 shows the BATSE All-Sky Plot of isotropical spatial distribution of 2704 gamma ray bursts observed during nine years. If GRB were to occur in the Milky Way galaxy, it would have been found in the thin plane of our galaxy instead they were found all over the sky [27].

The gamma-ray bursts were discovered accidentally by military satellites while looking for nuclear explosions in the late '60s. In 1967, Vella satellites detected the first GRB explosion unlike any gamma ray from a nuclear explosion while checking for gamma-ray emission due to nuclear weapon test. Later hundreds of bursts were recorded for three decades by the Compton Gamma Ray Observatory, Beppo-SAX, and HETE-2, but their nature and origination had not been determined. Identification of the precise location of GRB origin was very hard due to the short duration of the burst and the satellites were not equipped to move fast. This made it difficult to detect counterparts at any wavelength.

By the late 1990s, it became important to know the origin, distance, progenitor and the spectral characteristics of GRB as it will allow the astronomer to have a deeper understanding of the source of such GRBs. In 1996, Beppo SAX was launched by Italian Space Agency in collaboration with Netherlands Agency for Aerospace

Programs. It discovered the first X-ray afterglow of a GRB970228 and has been able to detect, localize, and follow up some GRBs before it landed in Pacific ocean in April 2003. Using the optical afterglow and the redshift of the source of GRB, the distance and luminosity of GRB were found. By observing and analyzing the afterglow of long-duration GRB970228 ($z=0.695$) and GRB980425/SN 1998bw ($z=0.0085$) discovered in 1997 and 1998 respectively, at X-ray and optical wavelength, the burst position of GRBs was found with sub-arcsecond precision. This breakthrough lead to a new era of GRB study. (Kouveliotu et al. 1990)

One of the many aspects that puzzled theorist at that time was the generation of gamma rays and X-rays in the first few seconds of the burst. The two emissions can be explained by the synchrotron shock model (SSM) (Rees & Meszaros, 1994) and the photospheric model (Rees & Meszaros, 2005; Pe'er et al. 2006; Beloborodov 2010a). In the SSM model, the shells with varying speed emitted by central engine collapse with one another and emit radiation in the process. This model explained the non-thermal spectra and light curve variability, but it does not agree with the observational relationships done by Amati (Amati, L. et al. 2002), Yonetoku (Yonetoku et al. 2004), and Golenetskii (Golenetskii et al. 1983) [27] [29]. The inconsistency in the SSM model lead to the consideration of an alternative model: photospheric model. In this model, the radiation is produced at high opacities deep within the jet and interacts with the matter in jet producing significant changes in

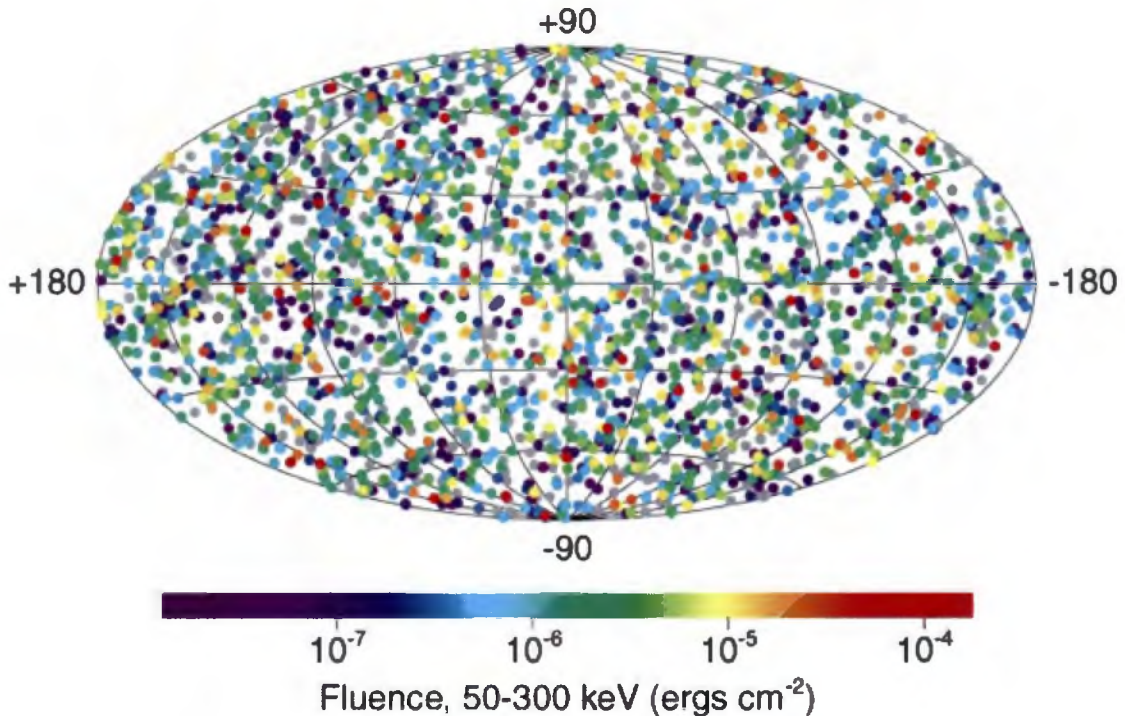


Figure 1.1: The figure shows the All-Sky plot of 2704 gamma ray burst locations detected by BATSE instrument over a nine-year period of observations. The bursts are isotropically distributed on the sky with a fluence of about 50-300 KeV. source: (NASA BATSE webpage)

the spectral energy distribution (SED). When the opacity is approximately 1, the radiation begins to decouple and escapes the jet. The photospheric model has been successful in agreeing with observational relationships [27].

In 2004, Neil Gehrels Swift Observatory (Gehrels et al.) was launched to understand the nature of gamma-ray burst. It carries three sets of instruments namely the Burst Alert Telescope (BAT); the X-ray Telescope (XRT) and the UV- Opti-

cal Telescope (UVOT). Within seconds of detecting the gamma ray emission of a GRB, it does a multi-wavelength search and transmits the location of GRB to the ground-based telescope in real time, which performs multi-wavelength (Optical, near infrared and radio) observations of the GRB at later times and deeper limits with respect to Swift capabilities. While Swift detects roughly 100 GRB/yr, the majority being long-GRB, it is also optimized to identify short Gamma-ray Bursts (around 25-30% of all GRB discovered). In 2005, Swift discovered a short GRB050509B afterglow at X-ray wavelength and a month later detected short GRB050709 at an optical wavelength. The location of these events coincides with the location of a low-redshift elliptical galaxy which showed that short GRB occurs mostly in older star population.

Hence, a ground-based rapid follow-up is very crucial for optical/NIR identification and then rapid spectroscopy ($1 < \text{day}$). This will allow us to deduce the key information about the GRB like redshift, the chemical composition of the interstellar medium. Studying about GRB and other fast transients has paved the way for time-domain astronomy, since we are already seen the flourish of dedicated facilities, like the Palomar Transient Factory, the Zwicky Transient Factory, and LSST, etc.

1.1.1 Long Gamma Ray Burst

Long GRB is produced due to the gravitational collapse of an extremely massive star which is 20 times more massive than the sun. This massive, fast-rotating star burns enough energy that its core becomes so massive making it unable to withstand its gravity and collapse into a black hole releasing jets of intensely bright radiation. Long gamma ray bursts have a duration greater than 2 seconds [30]. The interaction of blast wave and circumburst medium produced a longer-lived synchrotron emission called “afterglow”, which is detectable at X-ray through radio wavelength. Studying the afterglow unlocked an opportunity to localize the GRB at sub-arc-second precision.

The spectral energy distribution (SED) of afterglow provides information on the blast-wave kinetic energy, density and magnetic properties of the circumbursts environment. The progenitor of long GRBs are generally binary stars constitutes of a carbon-oxygen core with a neutron star (NS) companion. The core collapse of CO_{core} leads to a supernova explosion which in turn produces hypercritical accretion process on the NS companion. This process leads to the emission of X-ray flashes and binary driven hypernovae [31]. The GRB progenitors may produce stellar mass blackhole surrounded by accretion disk or a rapidly spinning, highly magnetized neutron star in the center [34].

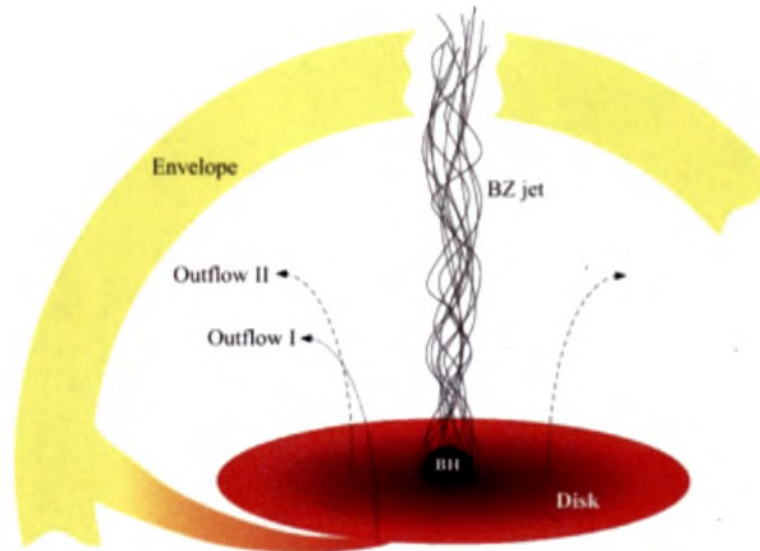


Figure 1.2: Schematic picture of BH hyperaccretion inflow-outflow model for LGRBs and ULGRBs. source: [34]

1.1.2 Short Gamma Ray Burst

Short GRBs are produced by the merging process of two compact objects such as two neutron stars or a neutron star – a black hole or a black hole – a black hole or white dwarf- white dwarf. The objects get trapped together by its gravity and rotate around each other emitting gravitational waves, losing energy and momentum. This leads to a loss in their orbital distance and collides violently with one another. The collision produces a jetted emission observed in the Gamma-ray energy range for a time between millisecond to 2 seconds [37]. Table 1.1 contains the summary of expectations of the progenitor models of short GRBs. By early 2000, the discovery

of long GRB became viable and its progenitors and explosion properties were studied, there was very less information about short GRB and its afterglow. Despite many searches, there was no detection of short GRBs afterglow, which lead to the fact that they may be very faint than the long GRB afterglow [21]. In 2005, shortly after the Swift was launched, short GRB050509B was found with an X-ray afterglow (Gehrels et al. 2006). The optical counterpart of GRB050509B was found with the precise location of the burst to be $10''$ in radius in an elliptical host galaxy at $z = 0.225$ (Gehrels et al. 2005; Bloom et al. 2006) [21].

Short GRBs are further classified as short gamma ray flashes and authentic short gamma-ray bursts. Short gamma-ray flashes are produced when the post-merger core does not exceed the NS critical mass and does not form into a blackhole. It has energy greater than 10^{52} ergs. Authentic short gamma-ray bursts are produced when the post-merger core reaches or exceeds the critical mass and gravitationally collapses to forms a blackhole. The energy of these bursts is greater than 10^{52} erg [31].

1.2 Gravitational Waves

Gravitational waves are disturbances in the curvature of spacetime due to the presence of accelerating mass. They propagate outward in the form of gravitational radiation at the speed of light. These occur due to the merger of heavy mass stars

Table 1.1: The table shows the predictions and expectations for short GRB progenitor models. Ref[21]

Testable Prediction	NS-NS/NS-BH	Massive Stars	WD-WD/WD-AIC
Spatial offsets	Substantial	Small	Small
Correlation with SF regions	Weak	Strong	Weak
Correlation with stellar mass	Weak	Strong	Strong
Host Demographics	Mix of elliptical and SF	SF only	Mix of elliptical and SF
Parsec-scale environment	Low densities(ISM/IGM)	High densities	Average densities(ISM)

such as double neutron stars or blackhole – neutron star or due to the collapse of stellar cores [24]. In 1916, Albert Einstein predicted the presence of gravitational waves and showed that an accelerating object of high mass would cause a wave-like distortion in space-time [2]. He concluded there must be three types of gravitational waves such as dubbed longitudinal – longitudinal, transverse – longitudinal, transverse – transverse waves. Einstein’s prediction was tested in 1974 when two astronomers from Arecibo Radio Observatory discovered a binary pulsar orbiting each other. The stars’ orbital period change was measured over eight years period and was determined that the stars were getting closer to each at the rate predicted by Einstein [2]. Gravitational waves have now been observed by LIGO and VIRGO experiments from September 14, 2015, when two supermassive black merged nearly 1.3 billion light-years away.

Gravitational waves are classified into four categories Continuous Gravitational Waves, Compact Binary Inspiral Gravitational Waves, Stochastic Gravitational



Figure 1.3: a)Image shows the artistic rendering of the gravitational wave. source:(Swinburne Astronomy Production). b)Image shows the aerial view of the VIRGO detector. VIRGO is the third detector to detect the gravitational wave. source:(ligo.caltech.edu/image)

Waves, and Burst Gravitational Waves.

Continuous gravitational waves are produced by a single massive and extremely dense object like a neutron star. These objects with any bumps or imperfections in its shape will generate gravitational waves as the star spins. These waves have the same frequency and amplitude and are hence called as continuous gravitational waves.

Compact binary inspiral gravitational waves are produced by massive and dense

binary objects orbiting in space such as white dwarf stars, black holes, and neutron stars. The duration of these waves depends on the mass of the objects as heavier massive objects like black hole produce short waves while lighter objects like neutron stars produce long waves. These compact binary systems are classified into three subclasses: Binary Neutron Star (BNS), Binary Black Hole (BBH), Neutron star-Blackhole Binary (NSBH).

Stochastic gravitational waves are small waves detected every direction in the sky and are called stochastic signals. These waves have a random pattern which makes it difficult to predict them precisely.

Burst gravitational waves are waves that are not yet detected or characterized. The waves for which the physics of the system are to be determined falls under this category [2].

The first gravitational wave observed was GW150914 on 14 September 2015, which was produced due to the merger of a binary black hole which supported the existence of a stellar-mass black hole. Two more gravitational waves were detected in late 2015 and eight more were detected in 2017 including the GW170817 which was accompanied by short gamma ray burst GRB170817A.

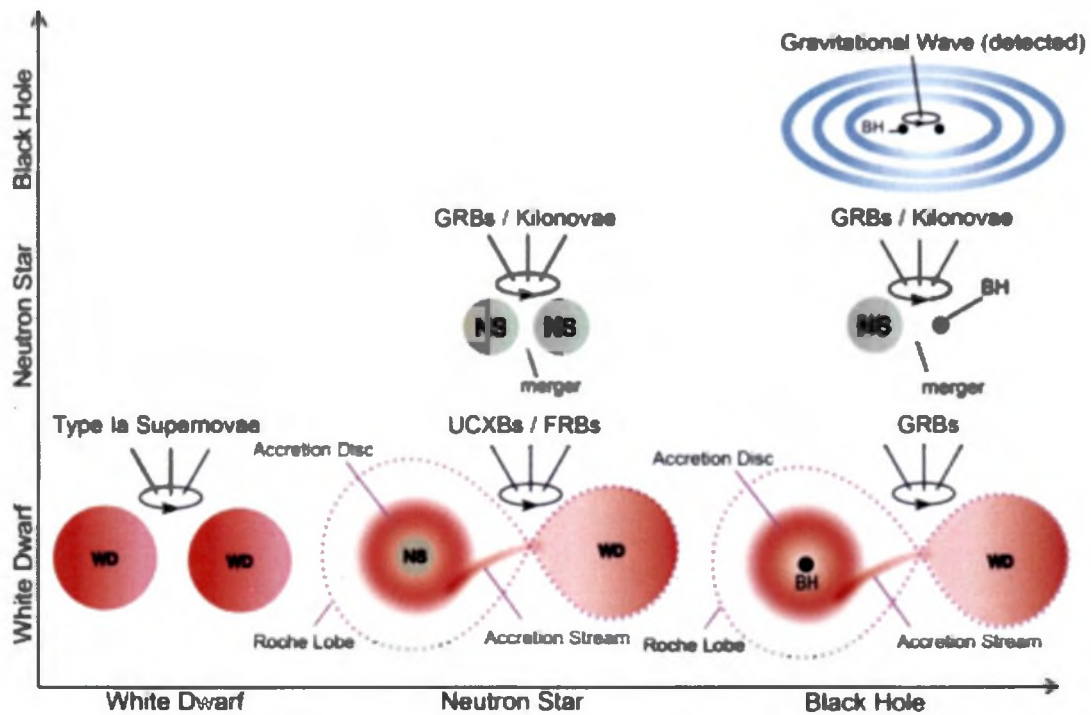


Figure 1.4: A full picture of compact binary systems. The figure shows different compact binary systems and potential corresponding observations. source: [20](Dong et al. 2018)

1.3 Fast Radio Burst

Fast radio burst is brief but intense bursts of radio waves of an unknown source which has a duration of few milliseconds. These bursts are bright, unresolved, with bandwidths nearly hundreds of MHz and detected all over the sky. In 2007, Lorimer et al. discovered the first radio burst which was called as “Lorimer Burst” [3]. The first radio burst was found to be located 3 degrees from the Small Magellanic Cloud

with a duration of fewer than 5 milliseconds and a dispersion measure of about 375 pc per cubic cm. In 2013, Thornton et al. discovered another four fast radio bursts which had dispersion measure of higher than Lorimer bursts with a range of up to 1000 pc cm^{-3} . In 2015, from archival data of Green Bank Telescope, FRB110523 was discovered which showed linear polarization and was found to be 6 billion light-years away. The large dispersion measure of the fast radio burst shows that FRBs are extragalactic or cosmological origin [22].

The nature of FRBs is unknown even though a good number of FRBs are reported which makes it study the distribution of FRB on the sky. There are several theoretical models of FRBs presents such as binary neutron star mergers (Totani 2013; Falcke & Rezzolla 2014; Zhang 2014; Cordes & Wasserman 2016; Zhang 2017), pulsars (Connor et al. 2016; Dai et al. 2016), black holes (Romero et al. 2016; Liu et al. 2016; Katz 2017), white dwarfs (Kashiyama et al. 2013; Gu et al. 2016), quark stars (Shand et al. 2016; Wang et al. 2018), magnetars orbiting black holes (Popov & Postnov 2013; Pen & Connor 2015; Metzger et al. 2017; Beloborodov 2017), etc, [22].

Some FRBs like FRB121102 exhibits a surprising repeating behavior. FRB 121102 is the only repeating FRBs detected by the Arecibo Observatory for which the host galaxy has been identified as a dwarf galaxy. The host galaxy has a redshift of 0.193 with the Very Large Array. Even though there have been many works done in the literature to study the FRBs, there is no way to analyze all properties of FRBs.

[33].

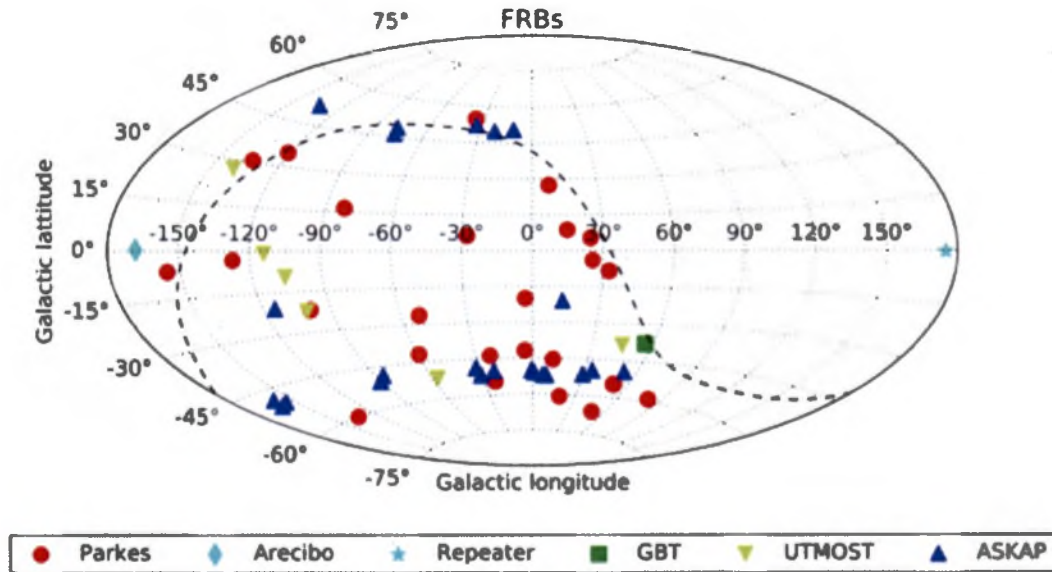


Figure 1.5: An Aitoff projected map of current FRBs in the Galactic coordinates, in which the black dashed line denotes the celestial equator. The detections are from these telescopes: Parkes radio telescope (red circles), Arecibo radio telescope (cyan thin diamond), Green Bank Telescope (green square), UTMOST (yellow down-pointing triangles), ASKAP (blue up-pointing triangles). In particular, the repeater (FRB 121102) is marked by a cyan star. source: [33](Yi et al. 2018)

Chapter 2

Robotic Telescope

A robotic telescope is a telescope that can be used without any human control thereby eliminating the constant presence of human to observe an object. This makes observation efficient and less costly due to reduced human interaction. These telescopes can be operated in queue mode, where the queue is set to optimizing the best observability for nightly targets. During this project, we utilized two semi-robotic telescopes, the RCT and VIRT, for which we designed a customizable data processing pipeline to process GRB data obtained from 2017 to 2019. The telescopes can be optimized to observe routinely a pre-fixed daily schedule, but they can respond to alerts generated on-board specific satellites (like Swift or Fermi) or the GW experiments. In the latter case, the schedule is interrupted and if the transient is visible, the telescope will put on hold the current observation from the queue and perform the required observations. Of specifically importance is the rapid-follow up of GRBs and FRBs, of which early data acquisition (typically a few minutes) allow

to better define the emission mechanism of the progenitor. The following are the two robotically controlled telescope for which the pipeline is coded to process the science image of GRB is taken using the telescope.

2.1 Robotically Controlled Telescope

Robotically Controlled Telescope(RCT) is a 1.3m (50") f/14 Cassegrain telescope located at Kitt Peak, Southern Arizona shown in figure 2.1(a). A CCD camera with 2048 x 2048-pixel SITe is used to capture the images. It contains Polycold compressor and closed circuit of supply and return lines for cooling which allows the camera to operate without maintenance over a large range of period. The CCD controller has a variety of operating modes such as readouts through a combination of up to 4 amplifiers, windowing and on-chip binning. The telescope has about 16 broadband and narrow-band filters and has two filter wheels available all times. The wheel 1 contains UBVRI filter sets, a red continuum filter and a narrow-band filter for H alpha and CN and the wheel 2 contains filters for NH2 and continuum, C2 and green continuum, C3 and blue continuum, together with narrow-band filters for SII and OIII. A third filter wheel currently holds filters for He II, H beta, NII, and SII. Other filters available include OH and UV continuum [4].

2.2 Virgin Island Robotic Telescope

Virgin Island Robotic Telescope (VIRT) is a 0.5m automated Cassegrain telescope located at the UVI observatory in St. Thomas, U.S. Virgin Islands shown in figure 2.1(b). The observatory was built in 1962 by Harry I Etleman as part of his private residence which later he donated to the College of the Virgin of the Island. The position of the telescope at the crest of the Crown Mountain gives an added advantage to observe the sky for any phenomenon between European and American boundaries. The telescope was installed in 2003. It is a 0.5m f/10 Cassegrain telescope that is mounted equatorially. The theoretical pointing precision of the telescope is about 0.1" for a field view of 20'. It contains 42-40 back-illuminated CCD camera with 2048 x 2048 13.5microm pixel provided by Finger Lakes Instruments. It has 12 position filter wheel which contains Johnson UBVRI and clear filters. Both the camera and the filter wheel are computer-controlled through a USB connection. In addition to observing the astronomical phenomenon, weather control study is done using the Davis professional weather station, and a Boltwood cloud detector. The dome of the observatory has a rotation speed of 6 degrees per seconds and is hurricane-proof. The program Talon developed by Optical Mechanics, Inc., is used to control the telescope. It is used to monitor the optical counterparts of the gamma-ray bursts; coordinated observing of various objects; and faculty and student research [25].

Both the RCT and VIRT is used to take a series of Bias, Dark, Flat and Science

images when GRB/GW emission is detected. These images once taken is to be processed further to study and analyze the GRB light curve. Presently these images are manually processed after the image is taken and stored in an archive. The pipeline is coded to reduce the manual work of processing the images, thereby making the work to be done automatically. The raw images containing the unwanted stripes of a black column on either side of the image is cropped initially to get the image containing actual science. This Bias and Flat image are then processed to get the median of the image and the median flat image is normalized to get even intensities of light in all pixels. The science images are then processed using the median bias and normalized flat images to get the final master science image. This processed master science image is free of noises. The master science images are then removed of any cosmic ray presence using Laplacian cosmic ray rejection technique. This image must be corrected for its coordinates since images were taken usually has a camera coordinate system. It is corrected for its world coordinate system (WCS). Now this WCS image is analyzed for the presence of gamma-ray burst using the DS9 software. If the gamma-ray electromagnetic counterpart is not seen on the processed science image, the set of processed science images are summed up to get a combined image. From this combined image, the limiting flux value for the GRB can be measured by calculating the calibrated magnitude using the instrumental magnitude and the zero point. The pipeline will be used to process these images and will be made compatible with the RCT. Using the help of the pipeline, the

images can be processed immediately as soon as it is captured thereby eliminating the manual processing of the images and reducing the processing time.

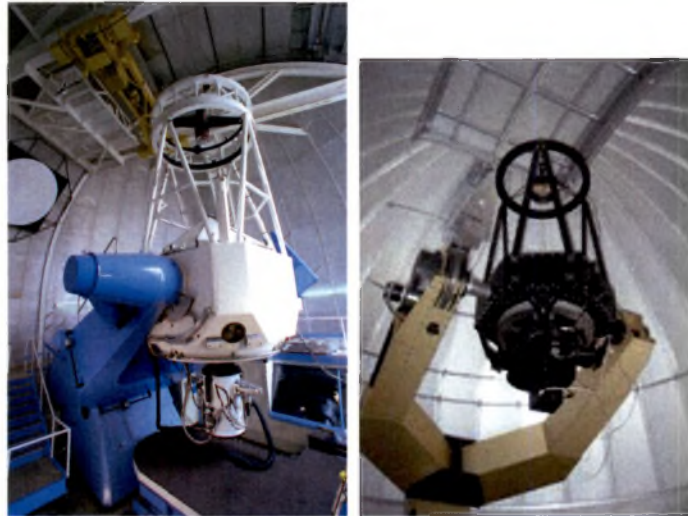


Figure 2.1: Image of a) Robotic controlled telescope at Kitt Peak and b) Virgin Island Robotic Telescope at US Virgin Island.

2.3 Charge Couple Device (CCD)

Charge-Coupled Device is an electronic device which collects light and converts into an electrical signal. It consists of a large number of light sensors or photosensitive pixels arranged in a 2-dimensional array. It is made up of the photoactive region or capacitor array and transmission region which is used to capture the image. The photoactive region is made up of silicone. Silicon has the property to trap and hold photon-induced charge carriers under appropriate electrical bias condition [5]. The

capacitor captures and accumulates electric charge proportional to light intensity when an image is made to project through the lens onto the capacitor array. The control circuit causes the capacitor array to transfer its content to the neighboring capacitor where the last capacitor is connected to a charge amplifier. This amplifier converts the electric signal into a sequence of voltage. This voltage is then sampled and digitized to get a digital image. It was the first imaging structure proposed by Michael Tompsett at Bell Laboratories for CCD imaging. Its functionings are divided into two phases namely exposure and readout. The CCD collects and stores the electrons when photons hit the pixels. During the exposure phase, these electrons are stored and then they get shifted down during the readout phase. The electrons are collected continuously during this readout stage. Once the CCD is read, the electrons at the lower-left cell are sent to the computer for further analysis. The rest of the electrons are shifted by one cell until all the pixels from the 1st line is processed. Then the next line gets shifted and then processed. This whole process continues until all the lines are shifted down and readout[6]. If the shifting is not fast enough, errors might occur due to the presence of light on the cells holding the charge during the transfer. The images also contain thermal noise and cosmic rays, due to which several exposures were taken with the CCD shutter closed and opened. Random noise in the image is removed by processing the images taken using shutters closed with the object image [17]. The CCD camera has a great dynamic range, spatial resolutions, spectral bandwidth and acquisition speed. It has high

performance due to its linear response over a wide range of light intensities [5]. CCDs are cooled usually to reduce the thermal noise. The use of CCD over classical film photography became prominent in astronomy due to its high spatial resolution, low noise and grain and auto exposure systems, convenience and flexibility in viewing the image as soon as it is taken and better sensitivity to light.

2.4 Photometric System

The photometric and spectroscopic system has a very important role in studying the stars and stellar system. During mid 20th century, the spectral classifications of stars were mostly done in MKK standards (Morgan, Keenan & Kellerman 1943). But the need to have a standardized photometry system became a prominent issue and many suggestions were put forth with no conclusion. During this time Johnson started to observe many stars and clusters using his UBV system which later became the standardized international photometric system [36]. The photometric system is a pass-band or filter whose sensitivity to incident radiation is known. The sensitivity of the system depends on the optical system, detectors and the type of filters used. Johnson photometric system is a wideband photometric system used to classify the stars according to their colors. It contains the ultraviolet (U), blue (B) and visual (V) magnitude filters. The B band is used to get the raw photographic magnitude, the V band gives the visual magnitude and the U band gives the additional band between B and the atmospheric cutoff [26]. Its important features are

U filter which is very useful in studying the hot stars and metallicity effects, and the short-wavelength cut-off which gets defined by the transmission function of the filters [36]. The CCDs are also coupled with standard photometric filters. Here we present a short review, with particular emphasis on the filters adopted in VIRT and RCT cameras.

The RCT and VIRT use Johnson's photometric system to calculate the flux values. The magnitude of the sources is obtained from GCN circulars archive which is then corrected for its galactic extinction. These magnitude values are then used to find the flux and its upper limit. A light curve is plotted for the time $(t-T_0)$ and the flux for each GRBs.

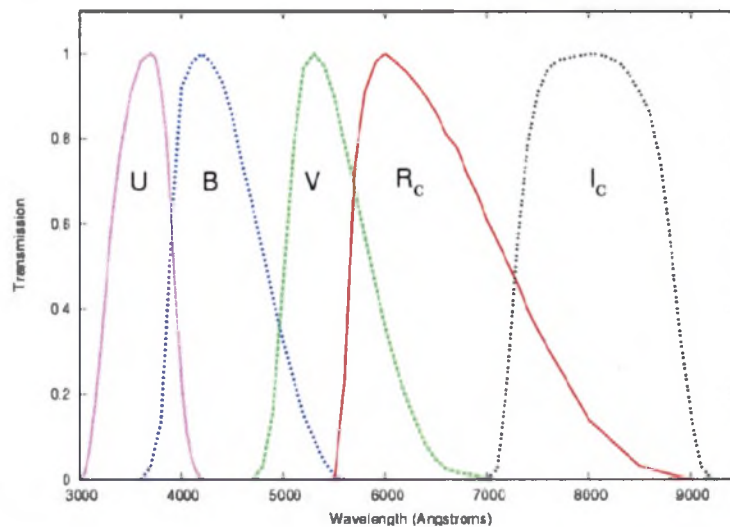


Figure 2.2: Plot shows the passband of Jonson–cousin filter. source: [35]

Chapter 3

Data Reduction Pipeline

The science image of the GRB source needs to be processed to remove any electric noise, different pixel sensitivity, random noise, hot pixels, dust, thermal noise, etc. In this reduction pipeline process, an effective method to process the science image is explained and the resulting processed master science image is shown in fig 3.1. The data reduction pipeline involves the following steps. Three images namely Bias image, Flat image, and Science image are used in the reduction pipeline process. The raw bias images and raw flat images are processed to get a median bias and flat image. The processed median flat image is then normalized to even out the pixel counts thereby producing a normalized flat image. Then a bias subtraction and flat fielding are done on the raw science image to obtain a processed science image. This science image is then processed to remove any cosmic rays present in it. This process gives the master science image completely or partially free of noises, pixel sensitivity or any dust present in the raw science image. Later its coordinates are

corrected for its world coordinate system using the nova.astrometry.net website.

3.1 Bias

The term bias is used to describe a CCD camera's pixel-to-pixel variation in zero points. Each pixel has a slightly different base value, and this bias is removed using a bias frame. Bias images (fig 3.2) are taken with the shutter closed at no or short exposure time. The images taken will have some readout and offset signal due to the variations in the camera sensors. To eliminate these variations from the science image, bias images are taken with zero-length exposure [7]. It is essentially an image taken by applying a constant voltage to the CCD detector [8]. In our case, ten sets of bias images are stacked together to find the median of the set. This median image is then subtracted from the science image to remove any readout noise present on the science image.

3.2 Flat

Flat images (fig 3.3) are used to avoid any optical imperfections due to vignetting caused by the optics and also to correct for sensor sensitivity variations. These images are taken with evenly illuminated source or shooting the sky at dawn or dusk at short exposure time and are stacked together to get the median of the images. This process corrects the uneven illumination on the science image when

processed [9]. Taking the image with short exposure length and cool CCD will help to reduce thermal noise. There are two types of flat fields taken: sky flats, dome flats. Sky flats are taken during twilight by focusing the telescope aperture at the sky during twilight while dome flats are taken by illuminating the dome in front of the telescope aperture using a projector lamp [10]. In RCT, dome flats are used to get the flat images. The median image is normalized further to get a steady light level or the same values in the master flat image [12].

3.3 Science

Science images (fig 3.4) are the actual image which contains the data of the object of interest that is to be processed. These images contain electric noise, different pixel sensitivity, random noise, hot pixels, dust, thermal noise, etc. We can partially mitigate (or sometimes eliminate) these effects by performing bias subtraction and flat fielding.

3.4 Processed Image

The raw bias and flat images are processed to get the median bias and flat image. The median flat image is further normalized to obtain a normalized flat image with the same pixel values. Then bias subtraction and flat fielding are done on the raw science image of the GRB source to get the processed science image free of noises

and pixel sensitivity. This science image is further processed to remove any cosmic rays present in it. The images below (fig 3.5) shows the median bias, median flat, normalized flat and fully process science image of GRB 180224A.

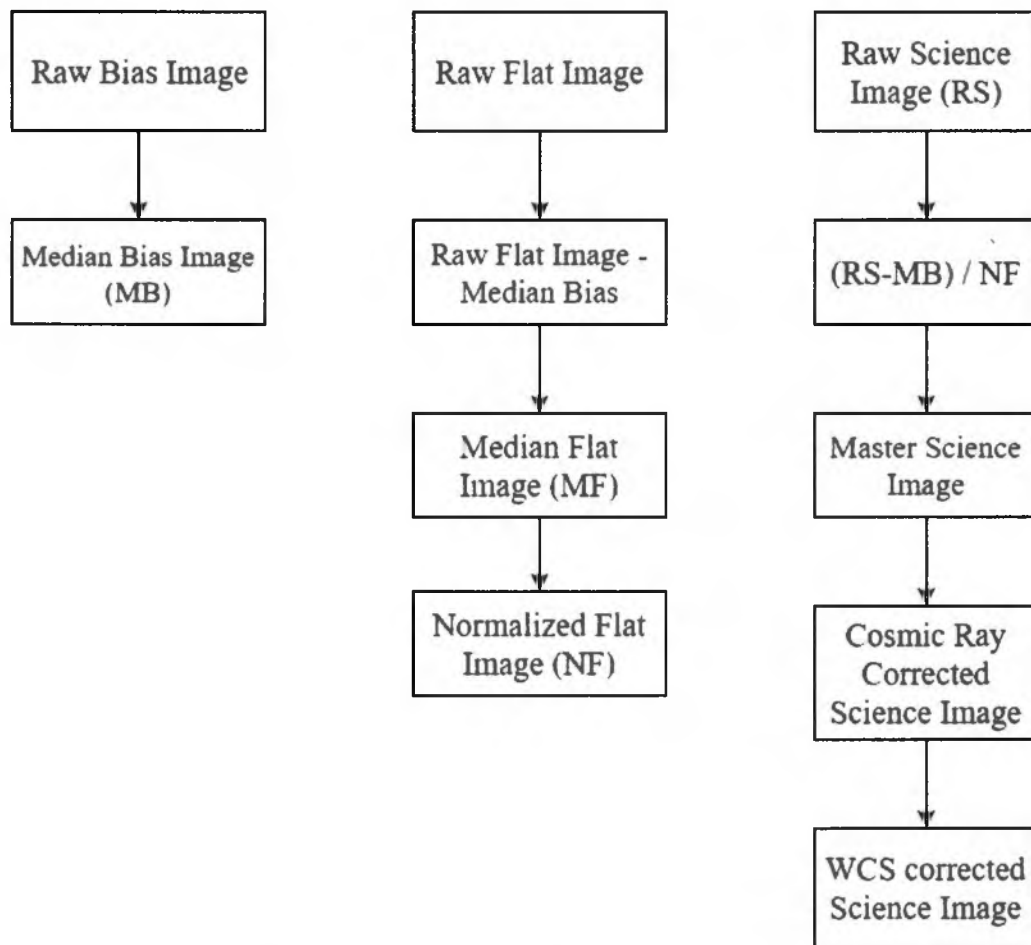


Figure 3.1: The flowchart shows the pipeline process for reducing the images to obtain the processed master science image which will be analyzed further to study the GRBs.

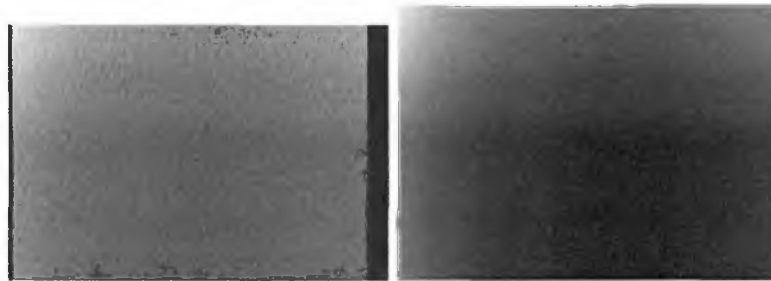


Figure 3.2: a) The raw bias image taken with shutter of the camera closed. It is used to reduce the variations in the signal due to camera sensors. The two black stripes on the right and left are due to the instrumental error. b) Bias image with the stripe removed on either side.

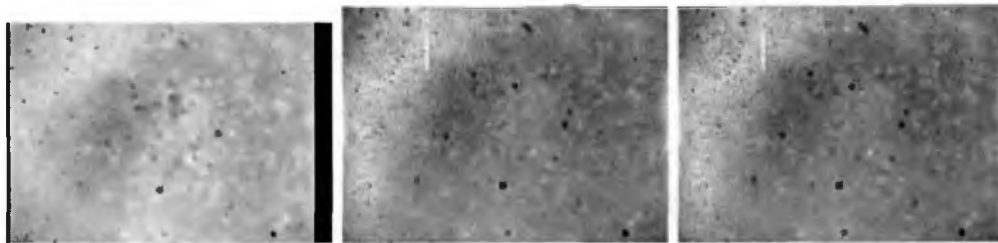


Figure 3.3: a) Raw flat Images taken in different filters B, V, R respectively. Flat images are taken with the source evenly illuminated. The grey stripes are due to the instrumental errors. This raw image is then processed to get median and then normalized to get same intensity level.

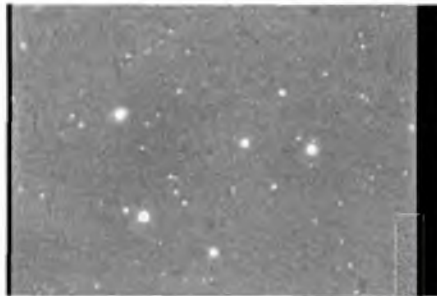


Figure 3.4: The figure shows the raw science image taken by the robotic controller telescope (RCT) at Kitt Peak using V filter.

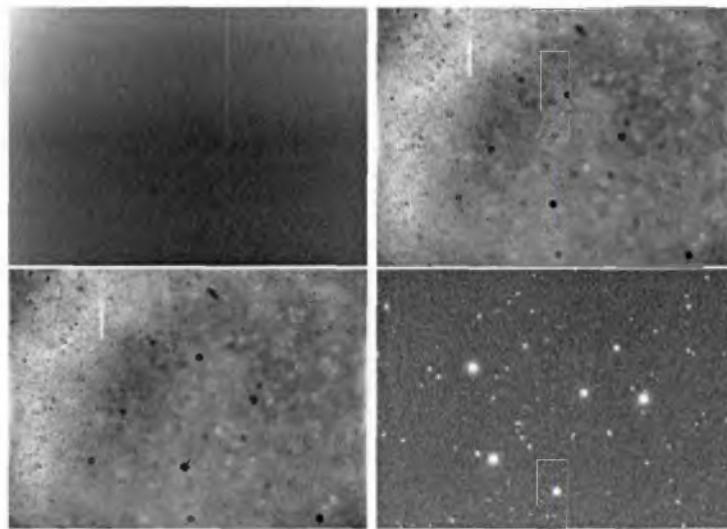


Figure 3.5: The image at the top left is a Median Bias image. A set of raw bias images are processed to get the median of the raw images which will eliminate readout noise in the science image. The image at the top right is the median flat image. A set of raw flat images are processed to the median flat. The image at the bottom left is the normalized flat image. The median flat image is normalized to get even intensity of light at every pixel. The image at the bottom right is the final master science image.

Chapter 4

Data Analysis

The data for RCT and VIRT images were obtained from WKU astronomy archive and Etleman Observatory respectively from October 2017 until June 2019 and data from the GCN archive were obtained for the same GRBs. The images from the RCT and VIRT were processed to get the master science image, completely or partially free from cosmic ray presence and was corrected for its world coordinate system. The pipeline process involves the following steps: A median bias image was obtained by finding the median for ten raw bias images of the same filter type. This median bias image is then subtracted from each raw flat images and then the median for the bias subtracted flat images of same filter type is obtained to get the median flat image. This median flat image is then normalized to get the normalized flat image. A bias subtraction and flat fielding were done on the raw science image of the same filter type as the flat image. This produces a master science image which is then processed to remove any cosmic ray presence and corrected for its world coordinate

system [11] [12]. From the master science image, a catalog magnitude was acquired from the USNO.B1 catalog using the ds9 software and an instrumental magnitude for the same RA and Dec of the catalog magnitude values were obtained using the SExtractor (Source Extractor) program. The two magnitude values from the image were subtracted to get the zero point for that image. The background count value for the GRB was used to find the upper limit (UL) of the instrumental magnitude of the GRB using the formula $UL = -2.5 * \log(3 * \sqrt{area} * \text{background count} / \text{Exposure time}) + 25$ where area is $\Pi * r^2$. The upper limit for the GRB magnitude is 3 sigma. Then the calibrated magnitude value is obtained by subtracting the upper limit value of the instrumental magnitude for the GRB and the zero point. The upper limit of the flux was found using the calibrated magnitude value through an online tool. This upper limit for the flux (mJy) is plotted against the time period in seconds to get the light curve of the GRB data obtained from the image. Then the magnitude value from the GCN archive is converted to its corresponding flux value using an online tool and then a light curve is plotted for this data [13] [15] [16]. Here is the detailed log [Table: 4.1] of the observations taken by VIRT and RCT, including the publicly available data obtained by GCN archive.

The tables [tables 4.2 - 4.13] below shows GRB name, the trigger time, filter used in the telescope, flux value and it's error of GRBs obtained from the GCN archive and from the images.

Table 4.1: Table below contains the list of GRBs analyzed, it's redshift and the telescope used to capture the science image of the particular GRB.

GRB	Redshift (z)	Telescope
GRB171010A	0.3285	Robotic Controlled Telescope at Kitt Peak
GRB171205A	0.0368	Robotic Controlled Telescope at Kitt Peak
GRB180224A		Robotic Controlled Telescope at Kitt Peak
GRB180205	1.4090	Robotic Controlled Telescope at Kitt Peak
GRB171120A		Robotic Controlled Telescope at Kitt Peak
GRB190627A	1.9420	Virgin Island Robotic Telescope

Table 4.2: Table shows the data obtained from the GCN archive about GRB171010A detected by RTC.

GRB	t-T0 (days)	Filter	Magnitude	Flux (mJy)	Notes	Reference
GRB171010A	0.30	<i>SDSS - I</i>	16.50 ± 0.02	0.88 ± 0.01	ICO 1m telescope observations	<i>GCN21991</i>
	0.62	<i>I</i>	17.85 ± 0.20	0.21 ± 0.01	optical observations	<i>GCN21988</i>
	0.62	<i>i</i>	20.31 ± 0.05	0.04 ± 0.01	optical observations	<i>GCN21988</i>
	1.23	<i>r</i>	19.18 ± 0.06	0.11 ± 0.06	Nordic Optical Telescope	<i>GCN22000</i>
	0.76	<i>Rc</i>	18.04 ± 0.16	0.31 ± 0.04	MITSuME Akeno Optical Observation	<i>GCN22001</i>
	0.76	<i>Ic</i>	17.33 ± 0.12	0.54 ± 0.06	MITSuME Akeno Optical Observation	<i>GCN22001</i>
	1.50	<i>R</i>	19.30	0.08	ESO New Technology Telescop	<i>GCN22002</i>
	0.86	<i>white</i>	18.84 ± 0.02	0.20 ± 0.01	Swift/UVOT Detection	<i>GCN22004</i>
	2.62	<i>r</i>	19.88 ± 0.02	0.06	RATIR Optical and NIR Observations	<i>GCN22011</i>
	2.62	<i>i</i>	19.59 ± 0.02	0.07	RATIR Optical and NIR Observations	<i>GCN22011</i>
	2.62	<i>Z</i>	19.25 ± 0.02	0.09	RATIR Optical and NIR Observations	<i>GCN22011</i>
	2.62	<i>Y</i>	19.19 ± 0.02	0.23 ± 0.01	RATIR Optical and NIR Observations	<i>GCN22011</i>
	2.62	<i>J</i>	18.97 ± 0.02	0.05	RATIR Optical and NIR Observations	<i>GCN22011</i>
	2.62	<i>H</i>	18.80 ± 0.03	0.03	RATIR Optical and NIR Observations	<i>GCN22011</i>
	0.56	<i>r</i>	18.00 ± 0.03	0.32	1.3m McGraw-Hill telescope	<i>GCN21987</i>

Table 4.3: Table shows the data obtained from the GCN archive about GRB171205A detected by RTC.

GRB	t-T0 (days)	Filter	Magnitude	Flux (mJy)	Notes	Reference
GRB171205A	0.37	R	18.00 ± 0.10	0.20 ± 0.01	LSGT optical afterglow follow-up observation	GCN22188
	0.37	I	18.10 ± 0.10	0.14 ± 0.01	LSGT optical afterglow follow-up observation	GCN22188
	0.37	Z	18.30 ± 0.20	0.21 ± 0.03	LSGT optical afterglow follow-up observation	GCN22188
	0.89	V	18.95 ± 0.15	0.10 ± 0.01	GOTO detection	GCN22190
	1.02	V	18.50 ± 0.10	0.16 ± 0.01	SMARTS optical/IR afterglow observations	GCN22192
	1.02	I	17.70 ± 0.10	0.21 ± 0.02	SMARTS optical/IR afterglow observations	GCN22192
	1.02	J	17.60 ± 0.10	0.16 ± 0.01	SMARTS optical/IR afterglow observations	GCN22192
	1.02	K	16.20 ± 0.10	0.21 ± 0.02	SMARTS optical/IR afterglow observations	GCN22192
	1.00	CR	18.2 ± 0.07	0.26 ± 0.02	CHILESCOPE optical observations	GCN22193
	1.60	B	20.70	2.66	GMG observations	GCN22195
	1.60	V	20.00	4.02	GMG observations	GCN22195
	1.60	R	20.70	1.64	GMG observations	GCN22195
	2.00	SDSS - R	19.43 ± 0.10	0.07 ± 0.01	LCO 1-m telescope observations	GCN22197
	2.00	SDSS - I	19.19 ± 0.10	8.52 ± 0.01	LCO 1-m telescope observations	GCN22197
	0.02	g'	19.10 ± 0.10	0.10 ± 0.01	GROND observations of the optical/NIR transient	GCN22198
	0.02	r'	18.90 ± 0.10	0.12 ± 0.01	GROND observations of the optical/NIR transient	GCN22198
	0.02	i'	18.90 ± 0.10	0.11 ± 0.01	GROND observations of the optical/NIR transient	GCN22198
	0.02	z'	18.80 ± 0.10	0.12 ± 0.01	GROND observations of the optical/NIR transient	GCN22198
	0.02	J	18.40 ± 0.20	0.08 ± 0.01	GROND observations of the optical/NIR transient	GCN22198
	0.02	H	18.20 ± 0.30	0.05 ± 0.001	GROND observations of the optical/NIR transient	GCN22198
	0.02	K	> 17.60	> 0.06	GROND observations of the optical/NIR transient	GCN22198
	0.02	white	18.05 ± 0.07	0.27 ± 0.02	Swift/UVOT Observations	GCN22202
	0.19	white	117.85 ± 0.05	0.33 ± 0.02	Swift/UVOT Observations	GCN22202
	2.21	white	18.58 ± 0.08	0.17 ± 0.01	Swift/UVOT Observations	GCN22202
	0.16	v	18.09 ± 0.08	0.25 ± 0.02	Swift/UVOT Observations	GCN22202
	0.60	v	18.26 ± 0.24	0.21 ± 0.04	Swift/UVOT Observations	GCN22202
	1.25	v	18.20 ± 0.12	0.22 ± 0.02	Swift/UVOT Observations	GCN22202
	0.04	b	18.69 ± 0.10	0.13 ± 0.01	Swift/UVOT Observations	GCN22202
	0.31	b	18.53 ± 0.06	0.15 ± 0.08	Swift/UVOT Observations	GCN22202
	0.57	b	18.43 ± 0.08	0.17 ± 0.01	Swift/UVOT Observations	GCN22202
	1.21	b	18.69 ± 0.08	0.13 ± 0.01	Swift/UVOT Observations	GCN22202
	0.004	u	17.75 ± 0.18	0.36 ± 0.06	Swift/UVOT Observations	GCN22202
	0.18	u	17.54 ± 0.06	0.44 ± 0.02	Swift/UVOT Observations	GCN22202
	0.57	u	17.66 ± 0.08	0.39 ± 0.03	Swift/UVOT Observations	GCN22202
	1.21	u	18.32 ± 0.09	0.21 ± 0.02	Swift/UVOT Observations	GCN22202
	1.12	uvm2	16.67 ± 0.06	1.15 ± 0.06	Swift/UVOT Observations	GCN22202
	3.29	J	18.50 ± 0.10	0.07 ± 0.01	UKIRT near-IR observations	GCN22215
	3.29	K	18.30 ± 0.10	0.03 ± 0.00	UKIRT near-IR observations	GCN22215
	0.60	uvm2	18.37 ± 0.15	0.24 ± 0.03	Swift/UVOT Observations	GCN22202
	1.25	uvm2	18.71 ± 0.11	0.18 ± 0.02	Swift/UVOT Observations	GCN22202
	0.15	uvm1	16.95 ± 0.06	0.81 ± 0.04	Swift/UVOT Observations	GCN22202
	0.58	uvm1	17.93 ± 0.10	0.32 ± 0.03	Swift/UVOT Observations	GCN22202
	1.21	uvm1	18.51 ± 0.11	0.19 ± 0.02	Swift/UVOT Observations	GCN22202
	0.20	uvm2	17.06 ± 0.07	0.80 ± 0.05	Swift/UVOT Observations	GCN22202
	1.05	uvm2	18.68 ± 0.08	0.18 ± 0.01	Swift/UVOT Observations	GCN22202
	1.25	uvm2	18.82 ± 0.12	0.16 ± 0.02	Swift/UVOT Observations	GCN22202
	0.92	J	16.70 ± 0.10	0.36 ± 0.03	TNG NIR detections	GCN22189
	0.64	R	20.40	0.02	GMG observation	GCN22186
	0.06	r	16.00	1.65	VLT/X-shooter observations	GCN22180
	0.01	white	> 19.60	> 0.07	Swift detection	GCN22177
	0.01	white_FC	18.10 ± 0.08	0.26 ± 0.02	Swift/UVOT Detection	GCN22181
	0.04	white	17.70 ± 0.09	0.38 ± 0.03	Swift/UVOT Detection	GCN22181
	0.01	u	17.78 ± 0.18	0.35 ± 0.05	Swift/UVOT Detection	GCN22181
	0.05	v	18.22 ± 0.15	0.22 ± 0.03	Swift/UVOT Detection	GCN22181
	0.04	b	18.45 ± 0.09	0.16 ± 0.16	Swift/UVOT Detection	GCN22181
	0.06	uvm1	17.13 ± 0.09	0.68 ± 0.05	Swift/UVOT Detection	GCN22181
	0.06	uvm2	17.11 ± 0.11	0.77 ± 0.07	Swift/UVOT Detection	GCN22181
	0.05	uvm2	16.96 ± 0.10	0.88 ± 0.08	Swift/UVOT Detection	GCN22181
	0.16	r	18.30 ± 0.05	0.21 ± 0.01	RATIR Optical and NIR Observations	GCN22182
	0.16	i	18.13 ± 0.02	0.23 ± 0.01	RATIR Optical and NIR Observations	GCN22182
0.16	Z	18.35 ± 0.05	0.18 ± 0.01	RATIR Optical and NIR Observations	GCN22182	
0.16	Y	18.13 ± 0.05	0.30 ± 0.01	RATIR Optical and NIR Observations	GCN22182	

Table 4.4: Table shows the data obtained from the GCN archive about GRB180224A detected by RTC.

GRB	t-T0 (days)	Filter	Magnitude	Flux (mJy)	Notes	Reference
GRB180224A	0.002	<i>white</i>	18.90 ± 0.07	0.11 ± 0.01	Swift/UVOT Detection	GCN22454
	0.03	<i>white</i>	20.70 ± 0.33	0.02 ± 0.01	Swift/UVOT Detection	GCN22454
	0.01	<i>v</i>	> 18.40	> 0.16	Swift/UVOT Detection	GCN22454
	0.01	<i>b</i>	> 19.50	> 0.06	Swift/UVOT Detection	GCN22454
	0.03	<i>u</i>	> 20.30	> 0.03	Swift/UVOT Detection	GCN22454
	0.01	<i>w1</i>	> 18.70	> 0.13	Swift/UVOT Detection	GCN22454
	0.01	<i>m2</i>	> 18.20	> 0.02	Swift/UVOT Detection	GCN22454
	0.01	<i>w2</i>	> 17.60	> 0.36	Swift/UVOT Detection	GCN22454
	0.05	<i>Rc</i>	> 20.20	> 0.03	0.5m telescope of the Osservatorio Astronomico	GCN22452
	0.45	<i>r</i>	22.94 ± 0.13	0.01	RATIR Optical Observations	GCN22446
	0.45	<i>i</i>	22.08 ± 0.06	0.01	RATIR Optical Observations	GCN22446
	0.45	<i>r</i>	22.56 ± 0.18	0.01	RATIR Optical Observations	GCN22446
	0.45	<i>i</i>	21.83 ± 0.14	0.01	RATIR Optical Observations	GCN22446

Table 4.5: Table shows the data obtained from the GCN archive about GRB180205A detected by RTC.

GRB	t-T0 (days)	Filter	Magnitude	Flux (mJy)	Notes	Reference
GRB180205A	0.605	<i>CR</i>	19.43 ± 0.06	0.06	Hankasalmi Observatory 0.4-m Richey-Chretien telescope	GCN22401
	0.054	<i>R</i>	18.00	0.19	1 - telescope at the Mt. LOAO and the 0.8m and 0.25 telescopes at the McDonald Observatory	GCN22397
	0.002	<i>white_FC</i>	15.75 ± 0.02	2.10 ± 0.04	Swift/UVOT Detection	GCN22396
	0.007	<i>white</i>	16.33 ± 0.02	1.23 ± 0.02	Swift/UVOT Detection	GCN22396
	0.004	<i>v</i>	16.11 ± 0.09	1.43 ± 0.11	Swift/UVOT Detection	GCN22396
	0.007	<i>b</i>	16.65 ± 0.07	0.84 ± 0.05	Swift/UVOT Detection	GCN22396
	0.007	<i>u</i>	16.82 ± 0.07	0.77 ± 0.05	Swift/UVOT Detection	GCN22396
	0.007	<i>uuw1</i>	16.04 ± 0.10	1.63 ± 0.15	Swift/UVOT Detection	GCN22396
	0.006	<i>uuw2</i>	16.32 ± 0.15	1.33 ± 0.17	Swift/UVOT Detection	GCN22396
	0.005	<i>uuw2</i>	17.06 ± 0.17	0.67 ± 0.10	Swift/UVOT Detection	GCN22396
	0.506	<i>R</i>	19.67 ± 0.10	0.04	Nanshan-1m optical observations	GCN22395
	0.579	<i>R</i>	19.97	0.03	Xinglong TNT optical observation	GCN22392
	0.885	<i>g'</i>	20.29 ± 0.03	0.03	2.2 m MPG telescope at ESO La Silla Observatory (Chile)	GCN22391
	0.885	<i>r'</i>	20.03 ± 0.03	0.04	2.2 m MPG telescope at ESO La Silla Observatory (Chile)	GCN22391
	0.885	<i>i'</i>	19.81 ± 0.03	0.05	2.2 m MPG telescope at ESO La Silla Observatory (Chile)	GCN22391
	0.885	<i>z'</i>	19.66 ± 0.03	0.05	2.2 m MPG telescope at ESO La Silla Observatory (Chile)	GCN22391
	0.885	<i>J</i>	19.47 ± 0.12	0.03 ± 0.01	2.2 m MPG telescope at ESO La Silla Observatory (Chile)	GCN22391
	0.885	<i>H</i>	19.16 ± 0.19	0.02 ± 0.01	2.2 m MPG telescope at ESO La Silla Observatory (Chile)	GCN22391
	0.009	<i>g'</i>	16.83 ± 0.01	0.75 ± 0.01	2.2 m MPG telescope at ESO La Silla Observatory (Chile)	GCN22383
	0.009	<i>r'</i>	16.68 ± 0.01	0.84 ± 0.01	2.2 m MPG telescope at ESO La Silla Observatory (Chile)	GCN22383
	0.009	<i>i'</i>	16.56 ± 0.01	0.93 ± 0.01	2.2 m MPG telescope at ESO La Silla Observatory (Chile)	GCN22383
	0.009	<i>z'</i>	16.38 ± 0.01	1.08 ± 0.01	2.2 m MPG telescope at ESO La Silla Observatory (Chile)	GCN22383
	0.009	<i>J</i>	16.22 ± 0.02	0.56 ± 0.01	2.2 m MPG telescope at ESO La Silla Observatory (Chile)	GCN22383
	0.009	<i>H</i>	16.05 ± 0.02	0.38 ± 0.01	2.2 m MPG telescope at ESO La Silla Observatory (Chile)	GCN22383
	0.009	<i>K</i>	16.08 ± 0.14	0.23 ± 0.03	2.2 m MPG telescope at ESO La Silla Observatory (Chile)	GCN22383
	0.885	<i>K</i>	> 17.60	> 0.06	2.2 m MPG telescope at ESO La Silla Observatory (Chile)	GCN22391

Table 4.6: Table shows the data obtained from the GCN archive about GRB171120A detected by RTC.

GRB	t-T0 (days)	Filter	Magnitude	Flux (mJy)	Notes	Reference
GRB171120A	0.232	<i>R</i>	21.50	0.01	the 2.16-m telescope located at Xinglong GWAC-F60A 60cm optical telescope MITSuME 50 cm telescope of Akeno Observatory MITSuME 50 cm telescope of Akeno Observatory MITSuME 50 cm telescope of Akeno Observatory Swift/UVOT observation Swift/UVOT observation	<i>GCN22145</i>
	0.260	<i>R</i>	19.50	0.05		<i>GCN22141</i>
	0.136	<i>g</i>	> 21.50	> 0.01		<i>GCN22140</i>
	0.136	<i>Rc</i>	> 20.70	> 0.02		<i>GCN22140</i>
	0.136	<i>Ic</i>	> 19.80	> 0.05		<i>GCN22140</i>
	0.002	<i>white_FC</i>	> 19.90	> 0.04		<i>GCN22144</i>
	0.005	<i>u_FC</i>	> 19.70	> 0.05		<i>GCN22144</i>
	0.035	<i>white</i>	> 21.10	> 0.01		<i>GCN22144</i>
	0.041	<i>v</i>	> 19.10	> 0.09		<i>GCN22144</i>
	0.037	<i>b</i>	> 20.90	> 0.02		<i>GCN22144</i>
	0.069	<i>u</i>	> 20.70	> 0.02		<i>GCN22144</i>
	0.097	<i>w1</i>	> 21.00	> 0.02		<i>GCN22144</i>
	0.118	<i>m2</i>	> 21.00	> 0.02		<i>GCN22144</i>
	0.062	<i>w2</i>	> 21.00	> 0.02		<i>GCN22144</i>

Table 4.7: Table shows the data obtained from the GCN archive about GRB190627A detected by VIRT.

GRB	t-T0 (days)	Filter	Magnitude	Flux (mJy)	Notes	Reference
GRB190627A	2.100	<i>R</i>	20.04 ± 0.20	0.03 ± 0.01	Xinglong 2.16m optical observation	<i>GCN24907</i>
	1.300	<i>R</i>	19.54	0.04	2.4-meter optical telescope at Gao-Mei-Gu	<i>GCN24905</i>
	1.415	<i>r</i>	19.77 ± 0.10	0.06 ± 0.01	Nordic Optical	<i>GCN24904</i>
	1.375	<i>R</i>	19.34	0.05	Optical imaging by D50 from Ondrejov	<i>GCN24903</i>
	0.485	<i>H</i>	16.96 ± 0.10	0.17 ± 0.02	NIR imaging from Liverpool Telescope	<i>GCN24902</i>
	0.442	<i>r'</i>	17.70 ± 0.04	0.30 ± 0.01	CAFOS at the 2.2 m telescope of the Calar Alto Observatory	<i>GCN24901</i>
	0.104	<i>R</i>	16.44	0.75	2.4-meter optical telescope at Gao-Mei-Gu	<i>GCN24896</i>
	0.226	<i>R</i>	18.94	0.08	MASTER-SAAO robotic telescope	<i>GCN24895</i>
	0.375	<i>R</i>	17.54 ± 0.14	0.27 ± 0.03	Montarrenti Observatory	<i>GCN24893</i>
	0.375	<i>R</i>	17.64 ± 0.13	0.25 ± 0.03	Montarrenti Observatory	<i>GCN24893</i>
	1.2	<i>R</i>	17.92 ± 0.12	0.19 ± 0.02	Virgin Island Robotic Telescope	<i>GCN24894</i>
	0.001	<i>white</i>	17.31 ± 0.10	0.51 ± 0.04	Swift/UVOT observation	<i>GCN24889</i>
	0.001	<i>white</i>	17.16	0.59	Swift Burst Alert Telescope	<i>GCN24889</i>

Table 4.8: Table shows the data obtained from the master science image of GRB171010A detected by RTC.

GRB	t-T0 (days)	Filter	Magnitude	Flux upper limit (mJy)	Notes
GRB171010A	10.659	<i>R</i>	22.10	0.004	RTC
	10.661	<i>R</i>	22.05	0.004	RTC
	12.614	<i>R</i>	22.39	0.003	RTC
	12.616	<i>R</i>	22.58	0.003	RTC
	14.610	<i>R</i>	22.69	0.002	RTC

Table 4.9: Table shows the data obtained from the master science image of GRB171205A detected by RTC.

GRB	t-T0 (days)	Filter	Magnitude	Flux upper limit (mJy)	Notes
GRB171205A	19.226	<i>R</i>	22.31	0.003	RTC
	19.228	<i>R</i>	22.44	0.003	RTC
	19.229	<i>R</i>	22.31	0.003	RTC
	19.230	<i>R</i>	22.43	0.003	RTC
	19.231	<i>R</i>	22.36	0.003	RTC

Table 4.10: Table shows the data obtained from the master science image of GRB180224A detected by RTC.

GRB	t-T0 (days)	Filter	Magnitude	Flux upper limit (mJy)	Notes
GRB180224A	0.602	<i>R</i>	23.33	0.001	RTC
	0.604	<i>R</i>	23.24	0.001	RTC
	0.606	<i>R</i>	23.13	0.002	RTC
	0.608	<i>V</i>	22.82	0.003	RTC
	0.610	<i>V</i>	22.55	0.004	RTC

Table 4.11: Table shows the data obtained from the master science image of GRB180205A detected by RTC.

GRB	t-T0 (days)	Filter	Magnitude	Flux upper limit (mJy)	Notes
GRB180205	1.045	<i>R</i>	22.90	0.002	RTC
	1.047	<i>R</i>	22.88	0.002	RTC
	1.049	<i>R</i>	22.93	0.002	RTC
	1.051	<i>V</i>	23.19	0.002	RTC
	1.053	<i>V</i>	23.32	0.002	RTC

Table 4.12: Table shows the data obtained from the master science image of GRB171120A detected by RTC.

GRB	t-T0 (days)	Filter	Magnitude	Flux upper limit (mJy)	Notes
GRB171120A	2.955	<i>R</i>	18.82	0.001	RTC
	3.960	<i>R</i>	23.79	0.001	RTC
	4.953	<i>R</i>	23.66	0.001	RTC
	2.975	<i>I</i>	23.06	0.001	RTC
	4.977	<i>I</i>	22.49	0.002	RTC

Table 4.13: Table shows the data obtained from the master science image of GRB190627A detected by VIRT.

GRB	t-T0 (days)	Filter	Magnitude	Flux upper limit (mJy)	Notes
GRB190627A	0.550	<i>R</i>	21.39	0.008	VIRT
	0.551	<i>R</i>	21.45	0.008	VIRT
	0.551	<i>R</i>	21.45	0.007	VIRT
	0.552	<i>R</i>	21.19	0.009	VIRT
	0.552	<i>R</i>	20.99	0.011	VIRT

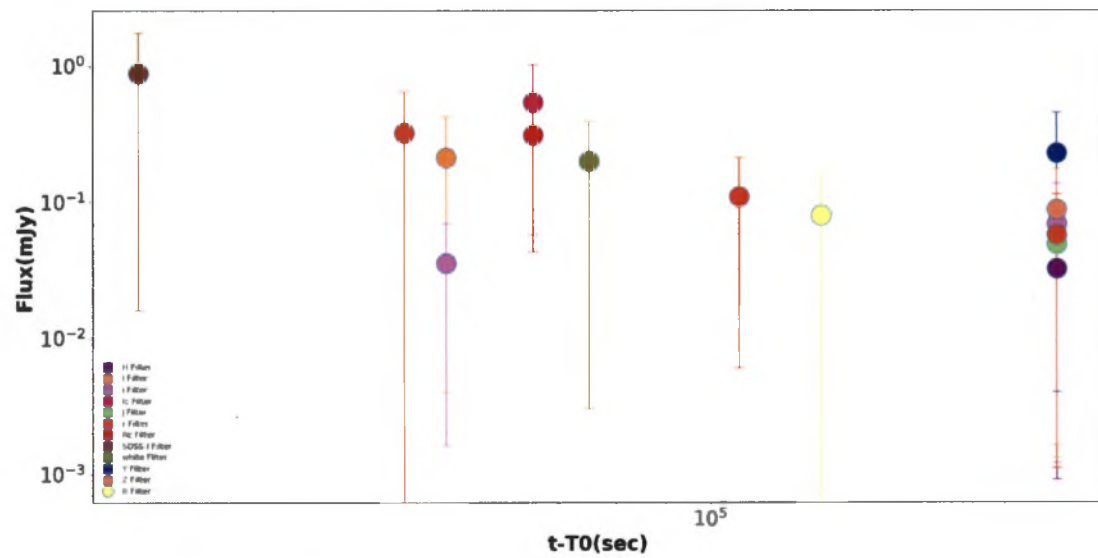


Figure 4.1: The plot shows the light curve of GRB171010A plotted using the data obtained from the GCN archive. The x-axis shows the time (sec) at which the GRB was observed by the observatories and the y-axis shows the flux in mJy. The magnitude and error in magnitude obtained from the GCN archive were corrected for its galactic extinction and then converted into its flux value [14].

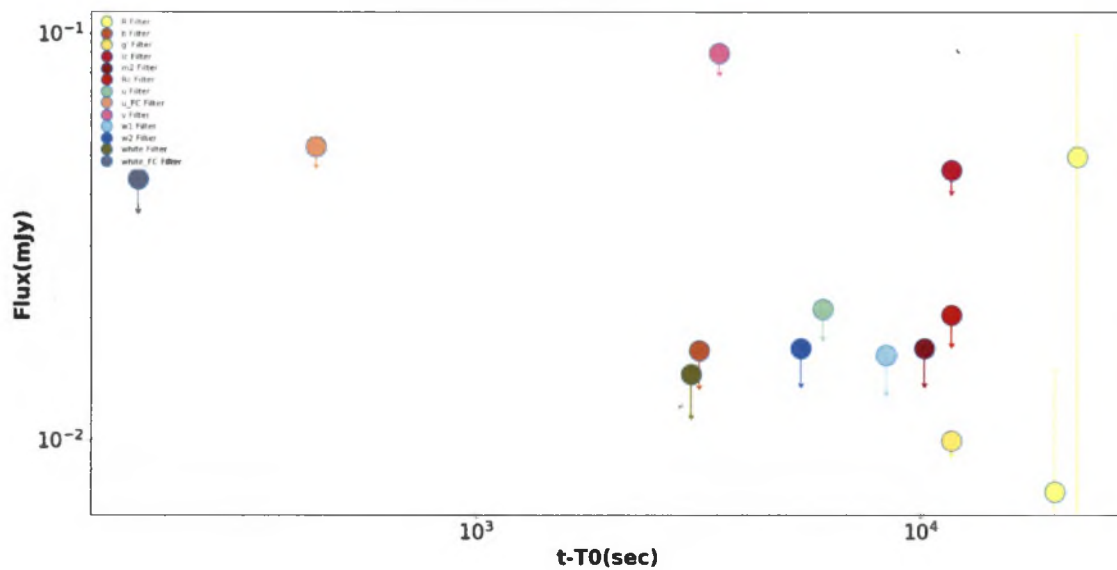


Figure 4.2: The plot shows the light curve of GRB171120A plotted using the data obtained from the GCN archive. The x-axis shows the time (sec) at which the GRB was observed by the observatories and the y-axis shows the flux in mJy. The magnitude and error in magnitude obtained from the GCN archive were corrected for its galactic extinction and then converted into its flux value.

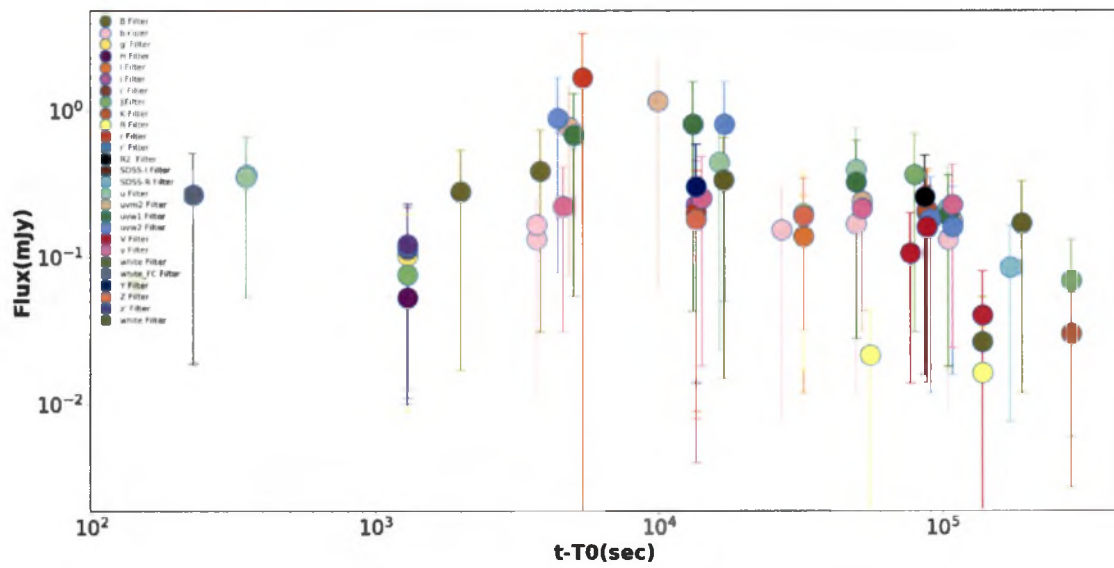


Figure 4.3: The plot shows the light curve of GRB171205A plotted using the data obtained from the GCN archive. The x-axis shows the time (sec) at which the GRB was observed by the observatories and the y-axis shows the flux in mJy. The magnitude and error in magnitude obtained from the GCN archive were corrected for its galactic extinction and then converted into its flux value.

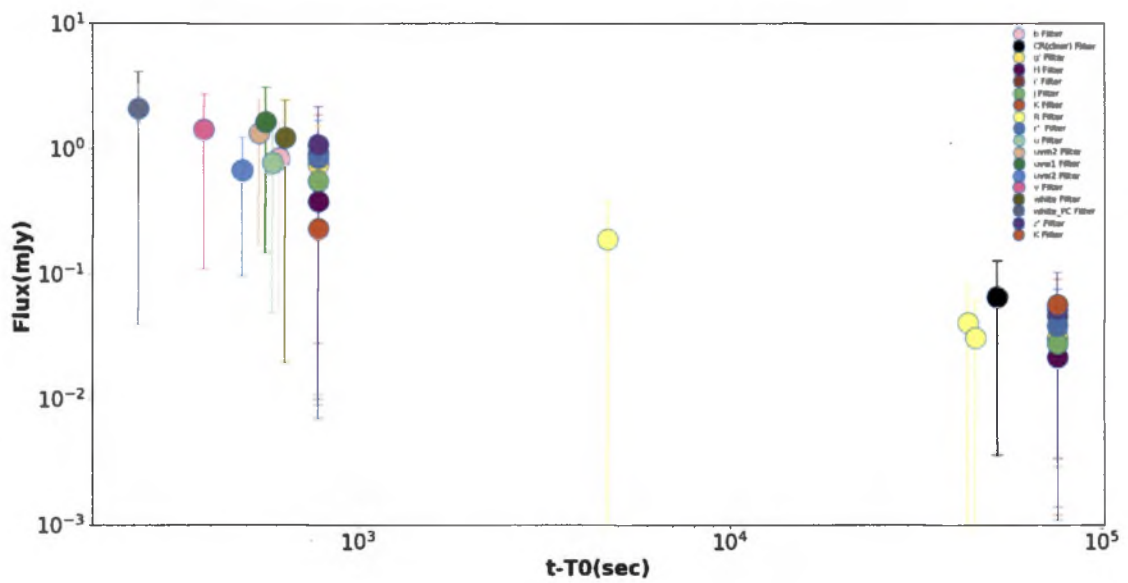


Figure 4.4: The plot shows the light curve of GRB180205A plotted using the data obtained from the GCN archive. The x-axis shows the time (sec) at which the GRB was observed by the observatories and the y-axis shows the flux in mJy. The magnitude and error in magnitude obtained from the GCN archive were corrected for its galactic extinction and then converted into its flux value.

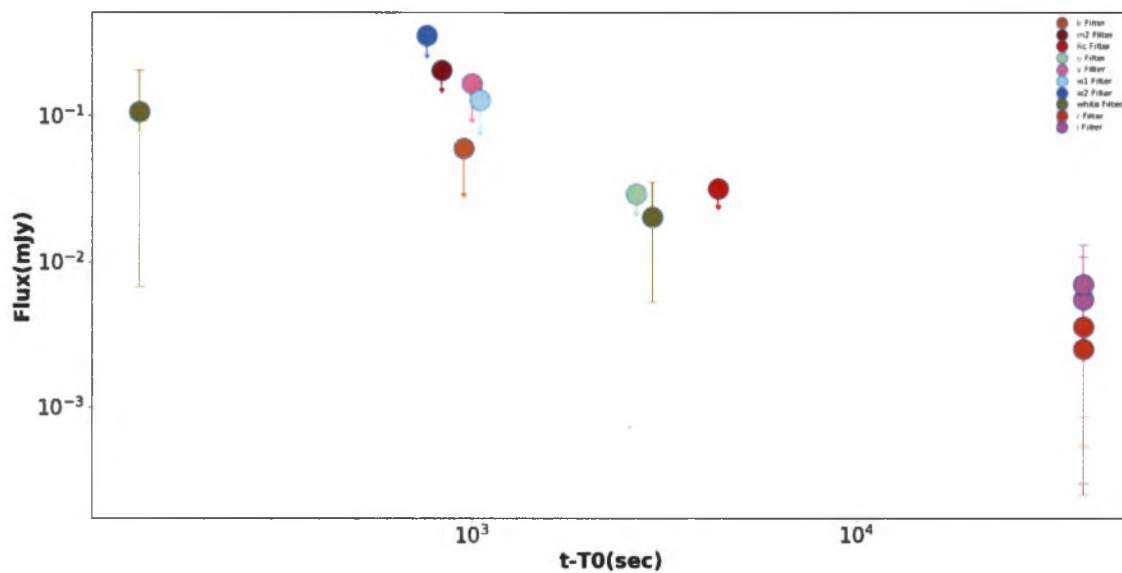


Figure 4.5: The plot shows the light curve of GRB180224A plotted using the data obtained from the GCN archive. The x-axis shows the time (sec) at which the GRB was observed by the observatories and the y-axis shows the flux in mJy. The magnitude and error in magnitude obtained from the GCN archive were corrected for its galactic extinction and then converted into its flux value.

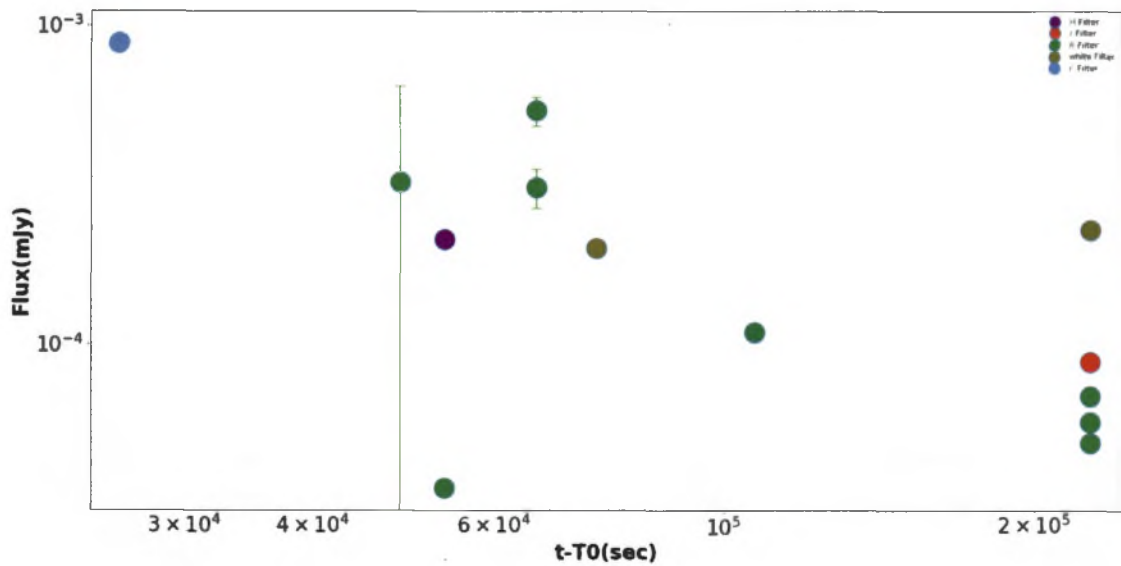


Figure 4.6: The plot shows the light curve of GRB190627A plotted using the data obtained from the GCN archive. The x-axis shows the time (sec) at which the GRB was observed by the observatories and the y-axis shows the flux in mJy. The magnitude and error in magnitude obtained from the GCN archive were corrected for its galactic extinction and then converted into its flux value.

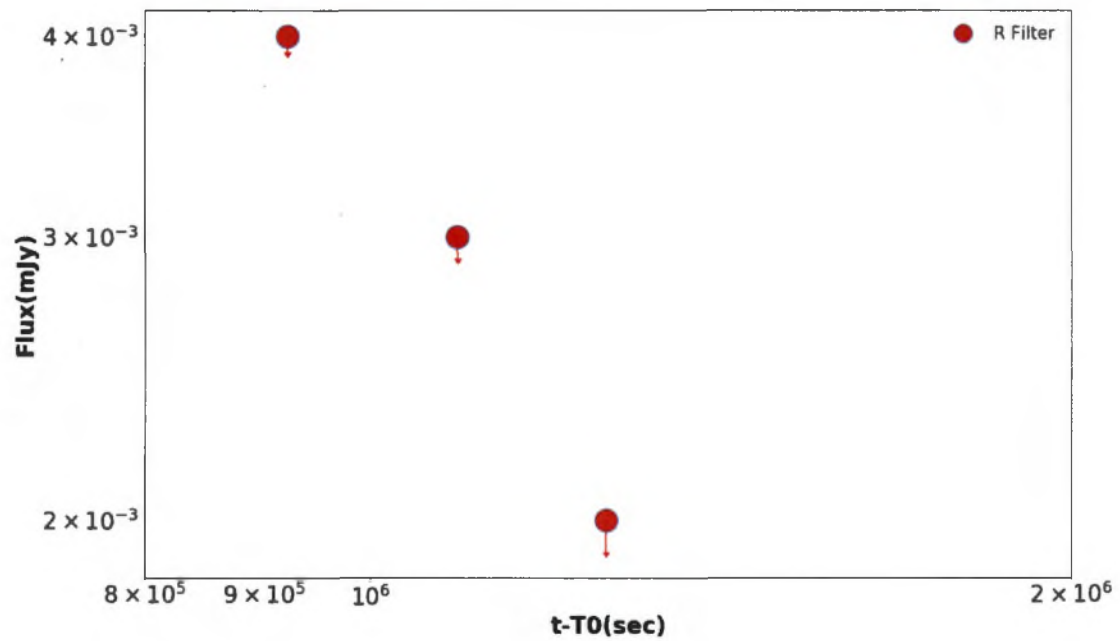


Figure 4.7: The plot shows the light curve of GRB171010A plotted using the data collected from the processed science image using SExtractor. The images are captured by the robotically controlled telescope at Kitt Peak. The x-axis shows the time (sec) at which the GRB was observed by the RCT and the y-axis shows the flux in mJy. The upper limit is calculated using the background count value of the area near the RA and Dec at which the source was detected.

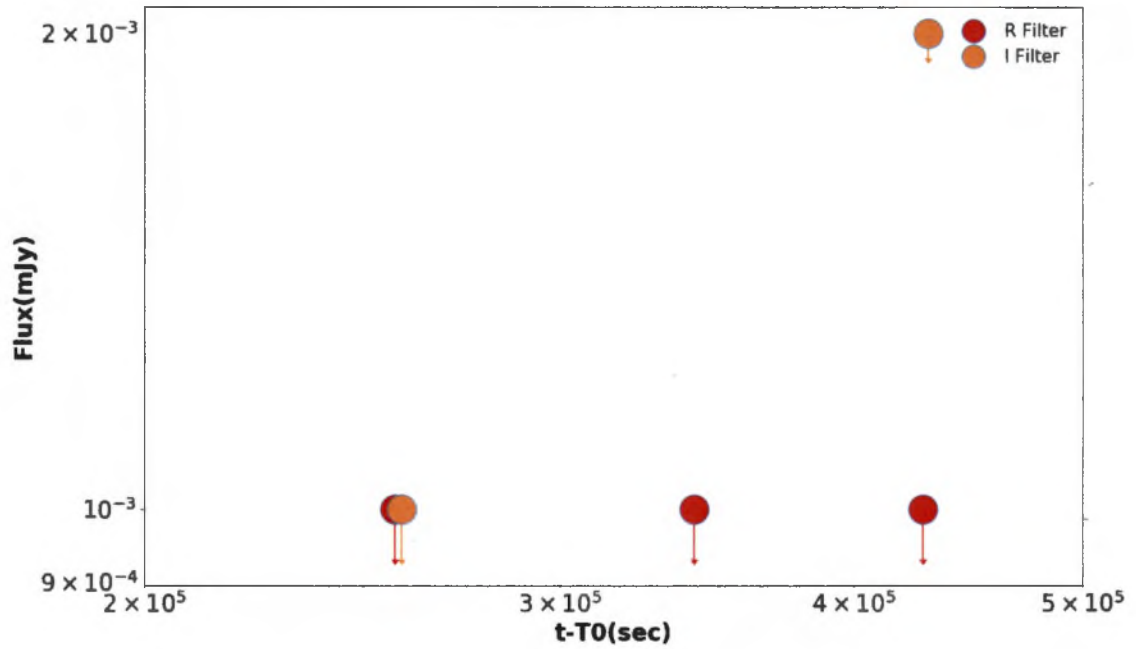


Figure 4.8: The plot shows the light curve of GRB171120A plotted using the data collected from the processed science image using SExtractor. The images are captured by the robotically controlled telescope at Kitt Peak. The x-axis shows the time (sec) at which the GRB was observed by the RCT and the y-axis shows the flux in mJy. The upper limit is calculated using the background count value of the area near the RA and Dec at which the source was detected.

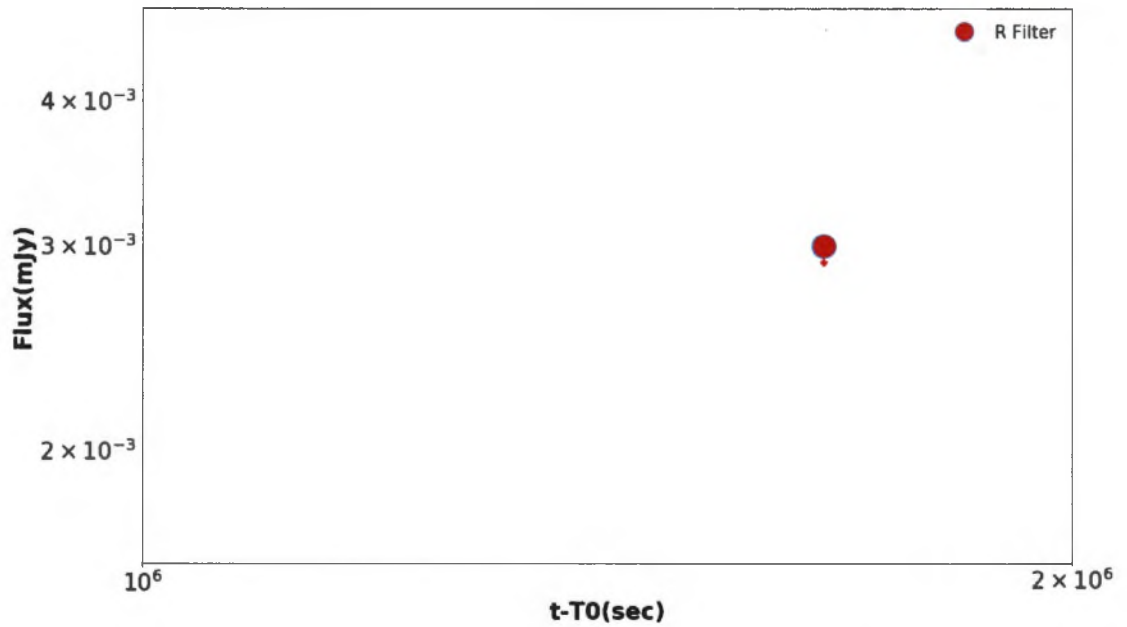


Figure 4.9: The plot shows the light curve of GRB171205A plotted using the data collected from the processed science image using SExtractor. The images are captured by the robotically controlled telescope at Kitt Peak. The x-axis shows the time (sec) at which the GRB was observed by the RCT and the y-axis shows the flux in mJy. The upper limit is calculated using the background count value of the area near the RA and Dec at which the source was detected.

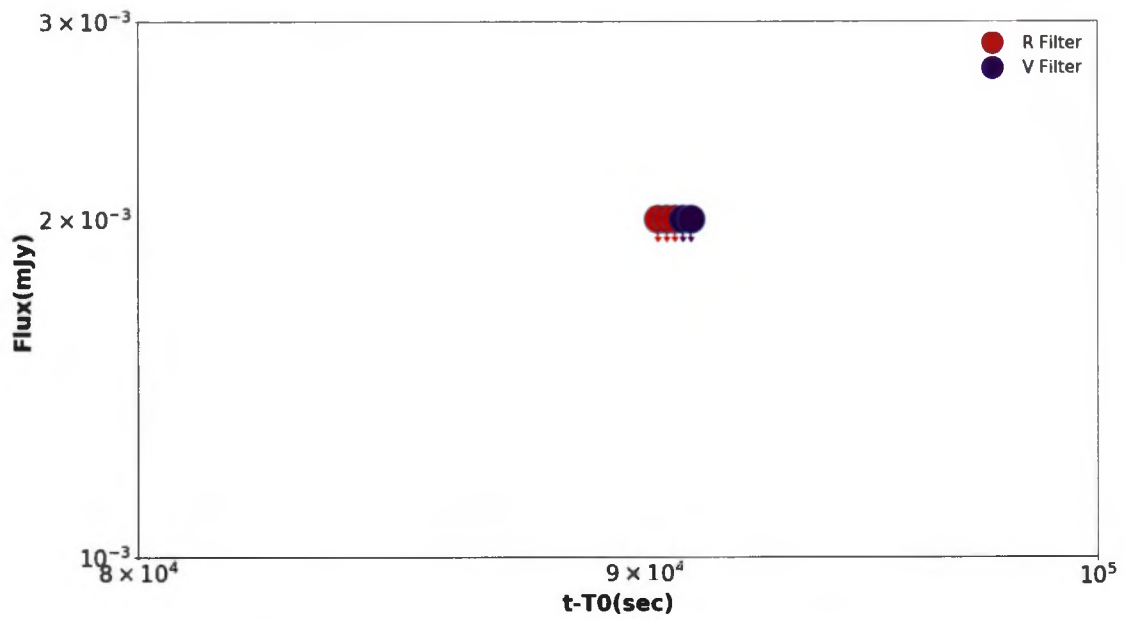


Figure 4.10: The plot shows the light curve of GRB180205A plotted using the data collected from the processed science image using SExtractor. The images are captured by the robotically controlled telescope at Kitt Peak. The x-axis shows the time (sec) at which the GRB was observed by the RCT and the y-axis shows the flux in mJy. The upper limit is calculated using the background count value of the area near the RA and Dec at which the source was detected.

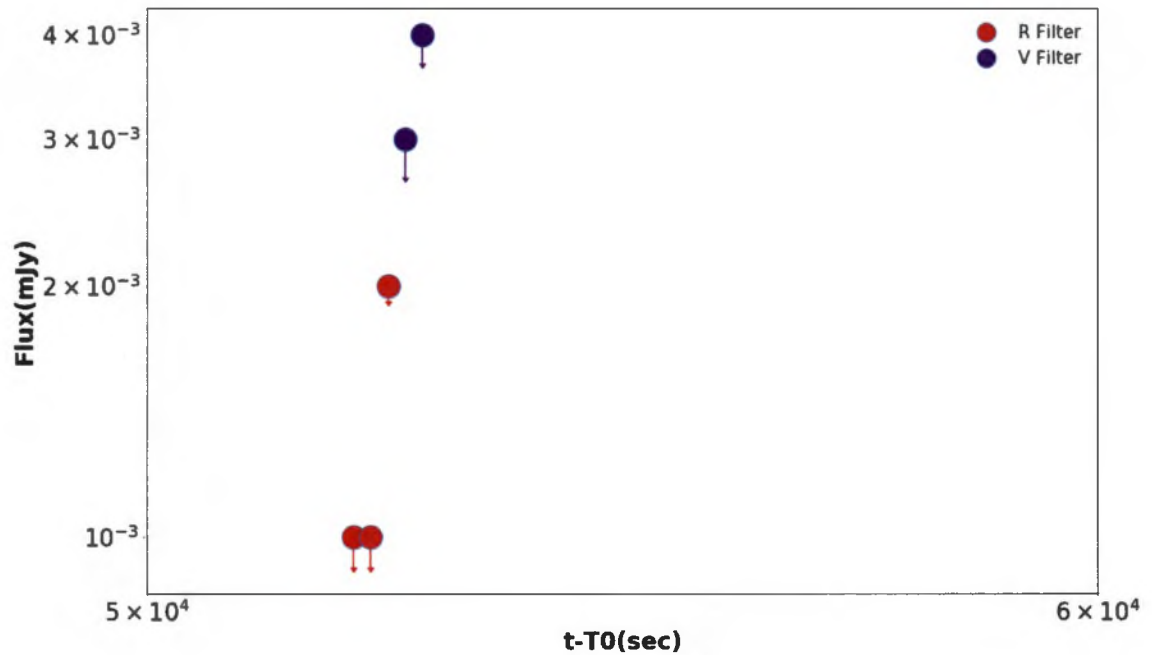


Figure 4.11: The plot shows the light curve of GRB180224A plotted using the data collected from the processed science image using SExtractor. The images are captured by the robotically controlled telescope at Kitt Peak. The x-axis shows the time (sec) at which the GRB was observed by the RCT and the y-axis shows the flux in mJy. The upper limit is calculated using the background count value of the area near the RA and Dec at which the source was detected.

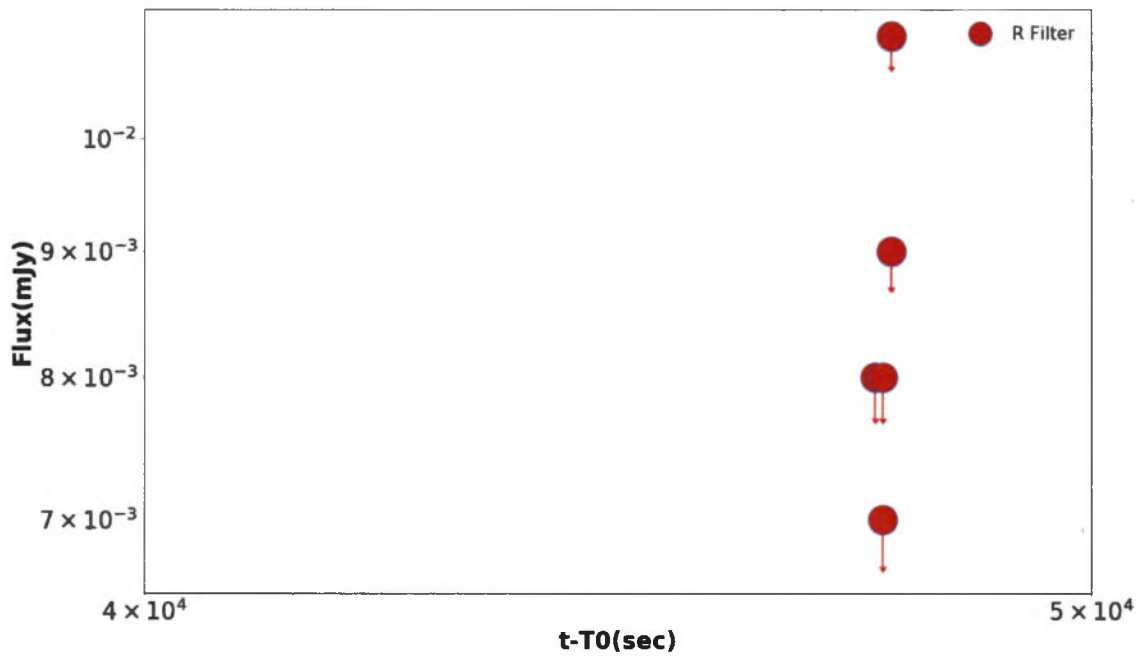


Figure 4.12: The plot shows the light curve of GRB190627A plotted using the data collected from the processed science image using SExtractor. The images are captured by the robotically controlled telescope at Kitt Peak. The x-axis shows the time (sec) at which the GRB was observed by the RCT and the y-axis shows the flux in mJy. The upper limit is calculated using the background count value of the area near the RA and Dec at which the source was detected.

Chapter 5

Conclusion

A reduction pipeline was successfully coded to get the final master science image by doing bias subtraction and flat fielding on the raw science image. Ten bias images and three to five flat images of the same filter type were processed to get the median bias and median flat images. The median flat image is further normalized to get the normalized flat image that evens out the pixel value in the flat image. Once the bias subtraction and flat fielding are done on the raw science image using the median bias and normalized image, the resulting image is then processed to remove any cosmic ray present on the raw science image. Thus the pipeline automatically processes and analyzes the data without any human interactions on the telescopes thereby providing a faster method to process the images as soon as it is captured by the telescope. This pipeline will allow the astronomers to do a further detailed analysis of the GRB and other fast astronomical sources.

The pipeline can be optimized for any telescope that observes the gamma-ray bursts

or other fast transients. In the future, the pipeline can be modified to select the flat images that have an average pixel count of about 20K to 50K. The master science image size is double the raw science image science which can be efficiently reduced to decrease the size of the resultant image.

Bibliography

- [1] <https://astronomy.fas.harvard.edu/transients>.
- [2] <https://www.ligo.caltech.edu/page/what/-are/-gw>.
- [3] <http://astronomy.swin.edu.au/cosmos/F/Fast+Radio+Bursts>.
- [4] http://rct.wku.edu/wordpress/?page_id=28.
- [5] <https://www.microscopyu.com/digital-imaging/introduction-to-charge-coupled-devices-ccds>.
- [6] <https://www.eso.org/~ohainaut/ccd>.
- [7] <http://www.rawastrodatab.com/pages/typesofimages.html>.
- [8] http://www.eso.org/~ohainaut/ccd/CCD/_proc.html.
- [9] <http://www.cfht.hawaii.edu/~baril/Pyxis/Help/flatdarkfield.html>.
- [10] <https://www2.keck.hawaii.edu/inst/common/DomeFlats.html>.
- [11] https://imageanalysis.readthedocs.io/en/latest/02/_master/_frames/cosmic/_ray.html.
- [12] <http://astrometry.net>.
- [13] https://gcn.gsfc.nasa.gov/gcn3_archive.html.
- [14] https://ned.ipac.caltech.edu/extinction_calculator.
- [15] http://www.stsci.edu/hst/nicmos/tools/conversion_form.html.

- [16] <https://www.gemini.edu/sciops/instruments/midirresources/imaging-calibrations/fluxmagnitudeconversion>.
- [17] Azeem Ahmad, Anand Kumar, Vishesh Dubey, Ankit Butola, Balpreet Singh Ahluwalia, and Dalip Singh Mehta., *Characterization of color cross-talk of ccd detectors and its influence in multispectral quantitative phase imaging.*, Optical Express, <https://doi.org/10.1364/OE.27.004572>.
- [18] Michael S. Bessell., *Standard photometric systems.*, Annu. Rev. Astron. Astrophysl.
- [19] Can-Min Deng, Yifu Cai, Xue-Feng Wu, and En-Wei Liang., *Fast radio bursts from primordial black hole binaries coalescence.*, Physical Review, <https://arxiv.org/abs/1812.00113v2>.
- [20] Yi-Ze Dong, Wei-Min Gu, Tong Liu, and Junfeng Wang, *A black hole - white dwarf compact binary model for long gamma-ray bursts without supernova association*, The Astrophysical Journal, <https://arxiv.org/abs/1712.02556v2>.
- [21] Wen-fai. Fong, *Unveiling the progenitors of short-duration gamma-ray bursts*, <http://nrs.harvard.edu/urn-3:hul.instrepos:12274595>.
- [22] Martin Houde, Fereshteh Rajabi, B.M. Gaensler, Abhilash Mathews, and Victor Tranchant., *Triggered superradiance and fast radio bursts.*, Monthly Notices of the Royal Astronomical Society, <https://doi.org/10.1093/mnras/sty3046>.
- [23] Tomoya Kinugawa, Yuichi Harikane, and Katsuaki Asano, *Long gamma-ray burst rate at very high redshift.*, The Astrophysical Journal.
- [24] Brian D. Metzger., *Kilonovae*, Living Rev Relativ (2017) 20: 3, <https://arxiv.org/abs/1610.09381v3>.
- [25] James Neff, D K. Allen, Dirk Aurin, T S. Boyajian, P Crowther, K Davis, D M. Drost, T W. Giblin, A Hurley, J Lucas, Harold Nations, and D Smith, *The virgin islands telescope: History and status*, Astronomische Nachrichten - ASTRON NACHR **325** (2004), 669–669.

- [26] Greg Ashton, Nikhil Sarin, Paul D. Lasky, *X-ray afterglows of short gamma-ray bursts: Magnetar or fireball?*, The Astrophysical Journal, <https://arxiv.org/abs/1812.08176v1>.
- [27] Tyler Parsotan, Diego Lopez-Camara, and Davide Lazzati, *Photospheric emission from variable engine gamma ray burst simulations*, The Astrophysical Journal, <https://arxiv.org/abs/1805.10327v2>.
- [28] Daniel A. Perley, *The fast, luminous ultraviolet transient at 2018cow: Extreme supernova, or disruption of a star by an intermediate-mass black hole?*, The Astrophysical Journal, <https://arxiv.org/abs/1808.00969v4>.
- [29] Pawan Kumar, Ramandeep Gill, Jonathan Granot, *Linear polarization in gamma-ray burst prompt emission*, The Astrophysical Journal, <https://arxiv.org/abs/1811.11555v2>.
- [30] Matteo Cantiello, Rosalba Perna, Davide Lazzati, *Ultra long gamma ray bursts from the collapse of blue super giant stars: An end-to-end simulation.*, The Astrophysical Journal.
- [31] J.A. Rueda, R. Ruffini, J. F. Rodriguez, M. Muccino, Y. Aimuratov, U. Barres de Almeida, C. L. Bianco L. Becerra, C. Cherubini, S. Filippi, M. Kovacevic, R. Moradi, G. B. Pisani, , and Y. Wang., *The binary progenitors of short and long grbs and their gravitational-wave emission.*, Joint International Conference of ICGAC-XIII and IK-15 on Gravitation, Astrophysics and Cosmology, <http://adsabs.harvard.edu/abs/2018EPJWC.16801006R>.
- [32] Arnon Dar, Shlomo Dado, *On the origin of supernova-less long gamma ray burst*, The Astrophysical Journal, <https://arxiv.org/abs/1710.02456v1>.
- [33] Rui Luo, Shu-Xu Yi, K.S. Cheng, *Clumpy jets from black hole-massive star binaries as engines of fast radio bursts.*, The Astrophysical Journal, <https://arxiv.org/abs/1811.11146v1>.
- [34] Cui-Ying Song and Tong Liu., *Black hole hyperaccretion inflow-outflow model. ii. long-duration gamma-ray bursts and supernova. ${}^5\text{6ni}$ bumps.*, The Astrophysical Journal, <https://arxiv.org/abs/1812.01708v1>.

- [35] Yamam Tawalbeh and Mashhoor Al-Wardat, *Modified orbital elements of the close visual binary systems hip11352, hip70973, and hip72479*, Ph.D. thesis, 05 2018.
- [36] Sidney van den Bergh., *Comments on the paper "fundamental stellar photometry for standards of spectral type on the revised system of the yerkes spectral atlas"* ., The Astrophysical Journal, <https://arxiv.org/abs/astro-ph/9906017v1>.
- [37] R. Margutti W.Fong, E. Berger and B. A. Zauderer., *A decade of short-duration gamma-ray burst broadband afterglows: Energetics, circumburst densities, and jet opening angles*, The American Astronomical Society.